

A micromechanical analysis of inter-fiber failure in long reinforced composites based on the phase field approach of fracture combined with the cohesive zone model

T. Guillén-Hernández · I.G. García · J. Reinoso · M. Paggi

Received: date / Accepted: date

Abstract The nature of failure in composites is strongly affected by damage at the microscale. The presence of different phases at different length scales leads to a significant complexity in the failure progression. At the micro scale, the complexity is due to the presence of different points of initiation for damage and the presence of cracks propagating both in the matrix and along the fiber-matrix interface. This scenario gives also the opportunity to improve the material design by modifying the properties of the different constituents in order to inhibit or delay some failure mechanisms. In view of this, the combination of the phase-field approach for fracture and the cohesive zone model is herein exploited to demonstrate its capability and accuracy for the study of failure initiation at the microscale.

Single-fiber problems subjected to transverse loading are considered as benchmark for the prediction of the sequence of stages of failure initiation, the size effect of the fiber radius on the apparent strength, the effect of a secondary tensile transverse load and the effect of a secondary neighbouring fiber. Numerical predictions are found to be in very good agreement with experimental trends and finite fracture mechanics solutions available in the literature.

1 Introduction

The spread in the use of fiber-reinforced polymeric composites (glass-based, GFRP, and carbon-based, CFRP) in many engineering applications with demanding requirements of high specific and strength ratios has motivated the development of efficient material characterization techniques starting from the micro-scale. At present, the level of exploitation of the load bearing capabilities of these materials is not yet fully optimized due to substantial difficulties in the understanding of the different failure modes affecting such materials.

In order to mitigate current limitations, in the last few years, substantial efforts have been conducted towards the development of high fidelity modeling techniques, which enable the achievement of a deeper level of characterization of the different failure mechanisms that govern the mechanical response of long

T. Guillén-Hernández
IMT School for Advanced Studies Lucca, Piazza San Francesco 19, 55100, Lucca, Italy
E-mail: teresa.guillen@imtlucca.it

I.G. García
Elasticity and Strength of Materials Group, School of Engineering, Universidad de Sevilla, Camino de los Descubrimientos s/n, 41092, Seville, Spain
E-mail: israelgarcia@us.es

J.Reinoso
Elasticity and Strength of Materials Group, School of Engineering, Universidad de Sevilla, Camino de los Descubrimientos s/n, 41092, Seville, Spain
E-mail: jreinoso@us.es

M. Paggi
IMT School for Advanced Studies Lucca, Piazza San Francesco 19, 55100, Lucca, Italy
E-mail: marco.paggi@imtlucca.it

fiber-reinforced composites. Particularly, the main modeling difficulties arise from the inherent heterogeneous character of GFRP and CFRP materials at the microscopic level, and from the fact that composite structures usually undergo progressive damage accumulation prior achieving macro-scale failure. Therefore, for reliable simulations, failure analysis of composite structures can be performed by means of progressive damage accumulation (PDA) techniques, whereby the distinction between damage onset and degradation phases are properly distinguished.

Complying with the PDA perspective, failure phenomena in GFRP and CFRP composites generally evolve at different length scales. On the one hand, physically-based models at the macro-scale foster the distinction between two main failure modes for laminate composites, i.e. interlaminar and intralaminar damage mechanisms. Seminal works triggering intralaminar failure events are rooted on the thermodynamics of irreversible processes (Maimí, Camanho, Mayugo & Dávila 2007), but they might require the use of very fine spatial discretizations of the structure (generally within the context of the finite element method, FEM) in order to adequately capture the damage phenomena under consideration (Puck & Schürmann 2004, Reinoso, Catalanotti, Blázquez, Areias, Camanho & París 2017, Quintanas-Corominas, Maimí, Casoni, Turon, Mayugo, Guillaumet & Vázquez 2018, Arefi & van der Meer 2018). The tremendous challenge for the development of reliable intralaminar failure models is revealed from the incorporation of the corresponding initiation criterion, whereby alternative formulations can be chosen. Concerning interlaminar failure, many of the existing investigations employ cohesive-based interface elements featuring different degradation schemes, being characterized by the traction separation law (TSL), upon complete delamination failure (Ortiz & Pandolfi 1999, Turon, Camanho, Costa & Renart 2010, Reinoso & Paggi 2014, Xu & Needleman 1994, Paggi & Wriggers 2012). Though these phenomenological approaches have been extensively used in the last two decades, they rely on input parameters which can be arduously determined by time-consuming and specific test campaigns.

On the other hand, current computational capacities have encouraged a new perspective of analysis through the exploitation of micro-mechanical models at the constituent level (Danzi, Fanterla, Panettieri & Palermo 2017, Herráez, Mora, Naya, Lopes, González & Llorca 2015, Tan, Naya, Yang, Chang, Falzon, Zhan, Molina-Aldareguía, González & Llorca 2018, Totry, Molina-Aldareguía, González & Llorca 2010, Van Der Meer 2016). These techniques have emerged as powerful and high-fidelity modeling tools which enable the generation of failure envelopes for different loading conditions. Moreover, micro-mechanical models allow a considerable reduction of the number of material parameters that characterize the mechanical response, and they can provide a more profound understanding of the physical phenomena under investigation. Within this framework, experimental data from the fiber and matrix, in terms of stiffness and strength properties, are used to study the constitutive behavior and for the determination of the corresponding macroscopic properties. The key concept of micro-scale simulations is the definition of the RVE domain (statistically representative volume element) which can be generated either using statistical method or by direct reproductions from microscopic images of the samples (Arteiro, Catalanotti, Melro, Linde & Camanho 2014). In this setting, experimental observations have evidenced the initial failure mode at the micro-scale is generally governed by the fiber-matrix mode (also denominated as inter-fiber failure), generating an interface crack which subsequently kinks out towards the matrix. The initiation and the subsequent progression of failure modes has been thoroughly investigated using experimental techniques (Rodríguez, Molina-Aldareguía, González & Llorca 2012) and numerical strategies within the context of the coupled stress-energy criterion (also called Finite Fracture Mechanics) (García, Paggi & Mantič 2014), the Boundary Element Method (BEM) (Correa, Mantič & París 2008, Correa, París & Mantič 2014, Távara, Mantič, Graciani & París 2011, Távara, Mantič, Graciani & París 2016) via interface cracks and nonlinear FEM through interface finite elements (Távara, Reinoso, Castillo & Mantič 2018). The posterior migration of this crack event into the matrix has also attracted an increasing interest in the last few years since it is widely accepted that macroscopic inter-fiber cracks are originated by the coalescence of fiber-matrix debonds that propagate through the matrix (Totry et al. 2010, Zhuang, Pupurs, Varna, Talreja & Ayadi 2018, Zhuang, Talreja & Varna 2018). In this setting, most of the previous numerical micro-mechanics investigations have conducted rigorous simulations in which material nonlinearities in the matrix are taken into consideration by means of pressure-dependent plasticity models (Melro, Camanho, Andrade Pires & Pinho 2013). Therefore, the information associated with the equivalent plastic strain in the matrix can provide valuable estimations with regard to plausible inter-fiber crack paths. The potential of those micro-mechanical tools has been demonstrated in several studies, which enables capturing the micro-mechanical inter-fiber failure behavior under different loading

conditions (Melro et al. 2013), and the in-situ effect on strength response of ultra-thin ply laminates (Arteiro, Catalanotti, Melro, Linde & Camanho 2015).

1.1 Preliminary in-situ experimental results

To illustrate the problem of inter-fiber failure at the microscopic scale, several preliminary experimental tests have been conducted by the authors to analyze the response of CFRP composites subjected to uniaxial tensile loading transverse to the fiber direction. Fig. 1 shows a schematic representation of the experiments, which were carried out using a tensile stage (DEBEN 5000S) inside a scanning electron microscope (Zeiss EVO MA-15). This experimental setup allows the in situ characterization of the specimen response and fracture.

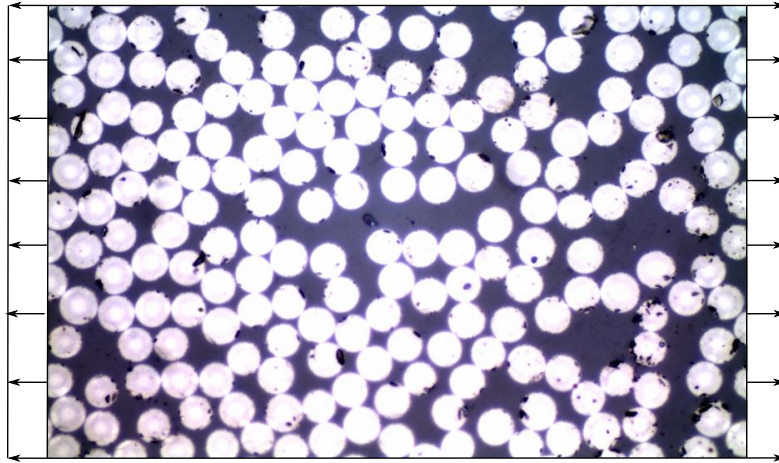


Fig. 1: Schematic of the experiments carried out.

As a result of the applied loading, in line with previous investigations (Correa et al. 2008, Távara et al. 2018, Totry et al. 2010), inter-fiber (matrix) failure is characterized by two main different stages at the microscale. In Stage 1, the specimen response features a linear elastic evolution load-displacement curve up to the appearance of small debonds at fiber-matrix interfaces (usually aligned with the prescribed loading) which grow unstably under Mixed Mode fracture conditions till reaching a critical debonding angle. Subsequently, in Stage 2, some of such interface cracks kink out into the matrix promoting their coalescence and leading to transverse macro-cracks in the ply which eventually can lead to catastrophic failure. This description is coincident with the experimental evidences obtained in our preliminary tests, as can be observed in Fig. 2.(a) (a careful description of those tests is beyond the scope of the present study). Moreover, performing a postmortem inspection using SEM imaging, it is even possible to observe some fibers totally separated from the main specimen, see Fig. 2.(b). These observations remark the need for a consistent approach to model the progression of cracks between the fiber-matrix interface and the matrix.

This preliminary study clearly shows the high complexity of the microscopic failure modes in long fiber-reinforced composites. Consequently, with the aim of exploiting their load bearing capacities, it is important to provide a deeper insight into the failure characteristics of such materials. This target can be achieved through the use of high fidelity micromechanical numerical models (mostly based on FE methods), which robustly capture the interface failure-matrix debonding and the subsequent kinking into the matrix and coalescence. The importance of capturing such inelastic effects at the microscale stems from the fact that macroscopic fracture in fiber-reinforced materials is generally the result of the evolution of localized microscopic cracks.

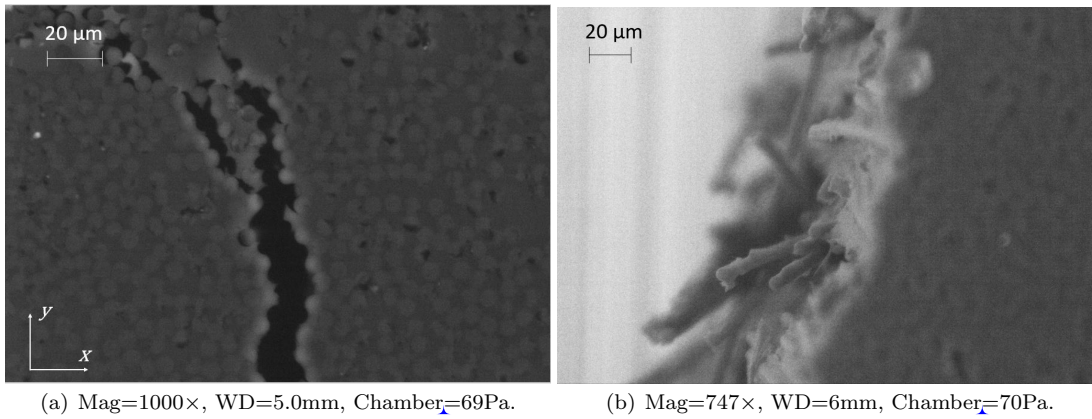


Fig. 2: SEM images of fracture of a unidirectional laminate of carbon-epoxy subjected to transverse loading. EHT=28.00kV, Signal=NTS BSD.

1.2 Objectives and outline

Differing from previous studies on the micromechanical response of long fiber-reinforced composites, the present investigation exploits an alternative modeling technique for micro-mechanical inter-fiber crack propagation, which relies on the use of the seminal approach combining the phase field (PF) method of fracture and the interface crack model approach proposed in (Paggi & Reinoso 2017) for heterogeneous media. In this setting, the phase field method of fracture falls into the category of gradient-enhanced (including nonlocal effects) (Comi 1999, Comi & Perego 2001), and its theoretical basis recalls the invocation of the so-called Γ -convergence problem (Bourdin, Francfort & Marigo 2000). Furthermore, as has been addressed in the related literature, the PF method provides a reliable and robust modeling tool which regularizes a sharp crack surface topology by means of the definition of a scalar-valued field denominated as the phase field damage variable (being possible to identify fully intact and broken states for any arbitrary point within the domain) (Miehe, Hofacker & Welschinger 2010, Miehe, Welschinger & Hofacker 2010). The salient aspects of the PF method concern that this modelling tool does not require any prescription concerning the crack nucleation location and the crack shape geometry; it allows triggering branching and coalescence events; and it is based exclusively on physically sound parameters. Its applicability for heterogeneous media in combination with interface cracks has been carried out for macroscopic simulations (Carollo, Reinoso & Paggi 2017, Carollo, Reinoso & Paggi 2018), see also the alternative approach relying on the level set method in (Nguyen, Yvonnet, Zhu, Bornert & Chateau 2016), and the new phase field formulation for interface failure proposed in (Hansen-Drr, de Borst, Hennig & Kstner 2019) which described the adhesive interfacial failure endowing an interaction between the interface width and the characteristic length scale of the bulk in a robust manner.

In view of such modelling potential, the current investigation delivers a novel attempt for triggering microscopic fracture events in fiber-reinforced composites. In particular, the matrix is assumed to obey an isotropic mechanical response, and inelastic effects due to damage are encompassed via an isotropic PF approach, whereas fiber-matrix decohesion is modeled using an interface model compatible with damage in the bulk. Thus, the objective of this paper is examining and validating the combined PF-CZM approach for the analysis of the micromechanical response of composites, and providing a deeper analysis concerning different crucial aspects that characterize the material response at this scale: (i) the prescribed external loading, (ii) size effects induced by the fiber radius, and (iii) the effect of the presence of a secondary fiber. These features at the microscopic scale are clearly interrelated to transverse crack formation processes, which generally lead to the laminate collapse at the macroscale.

The manuscript is organized as follows. In Section 2, the fundamentals of the phase field model for the bulk and its combination with the interface formulation are outlined. Section 3 represents a thorough numerical investigation analyzing the effects on the failure pattern of: (i) the prescribed external loading, (ii) size effect of the fiber radius, and (iii) the effect of the presence of a secondary fiber. Finally, the main conclusions of this investigation and the prospective research directions are drawn in Section 4.

2 Modeling strategy

This section outlines the basic concepts of the phase field (PF) approach of fracture (Miehe, Hofacker & Welschinger 2010) and the corresponding coupling with the interface cohesive zone formulation developed in (Paggi & Reinoso 2017).

2.1 Phase approach of fracture in the bulk

The forthcoming derivations are restricted to the infinitesimal deformation setting due to the scope of application in the current investigation. Nevertheless, suitable derivations for large deformations can be found in (Reinoso, Paggi & Linder 2017) and the references therein given.

In order to introduce the basic aspects of the PF approach of fracture in a multi-dimensional (2D or 3D) framework, we refer to an arbitrary solid in the Euclidean space \mathbb{R}^n is identified by $\mathcal{B} \in \mathbb{R}^n$, where n is the dimension of the analysis. A material point within the domain in the Cartesian setting is given by the position vector \mathbf{x} . Body actions are denoted by the vector $f_v : \mathcal{B} \rightarrow \mathbb{R}^n$. The boundary of the solid \mathcal{B} is identified by $\partial\mathcal{B} \in \mathbb{R}^{n-1}$, which is split into the boundary portions whereby the kinematic and static actions are prescribed, namely the regions $\partial\mathcal{B}_u$ and $\partial\mathcal{B}_t$, respectively, which are characterized by the corresponding fields $\bar{\mathbf{u}}$ and $\bar{\mathbf{t}}$. These parts of the body boundary fulfill the standard conditions: $\partial\mathcal{B}_t \cup \partial\mathcal{B}_u = \partial\mathcal{B}$ and $\partial\mathcal{B}_t \cap \partial\mathcal{B}_u = \emptyset$. Therefore, these prescribed actions can be expressed as:

$$\mathbf{u} = \bar{\mathbf{u}} \quad \text{on } \partial\mathcal{B}_u \quad \text{and} \quad \bar{\mathbf{t}} = \boldsymbol{\sigma} \cdot \mathbf{n} \quad \text{on } \partial\mathcal{B}_t, \quad (1)$$

where \mathbf{n} stands for the outer normal vector to the body.

The kinematics of the solid is characterized by the displacement field $\mathbf{u} : \mathcal{B} \rightarrow \mathbb{R}^n$. The Cauchy stress and the infinitesimal strain tensor fields are introduced as: $\boldsymbol{\sigma} : \mathcal{B} \rightarrow \mathbb{R}^{n \times n}$ and $\boldsymbol{\varepsilon} : \mathcal{B} \rightarrow \mathbb{R}^{n \times n}$. In the infinitesimal deformation setting, the strain field is defined as the symmetric part of the displacement gradient: $\boldsymbol{\varepsilon} := \nabla_{\mathbf{x}}^s \mathbf{u}$.

Rooted on the Griffith theory of fracture (Griffith 1921), the central aspect of the PF technique envisages a regularized crack representation of the sharp crack topology within a diffusive crack zone of width l . This regularization is characterized through the introduction of damage-like scalar variable $\vartheta : \mathcal{B} \times [0, t] \rightarrow [0, 1]$ (Tanné, Li, Bourdin, Marigo & Maurini 2018), which triggers the progressive stiffness degradation upon fracture evolution. This regularization is schematically depicted in Fig. 3 for a 1D problem (Miehe, Hofacker & Welschinger 2010, Miehe, Welschinger & Hofacker 2010), and it is characterized by the length l , usually known as the length scale parameter that controls the transition between fully intact ($\vartheta = 0$) and broken ($\vartheta = 1$) states.

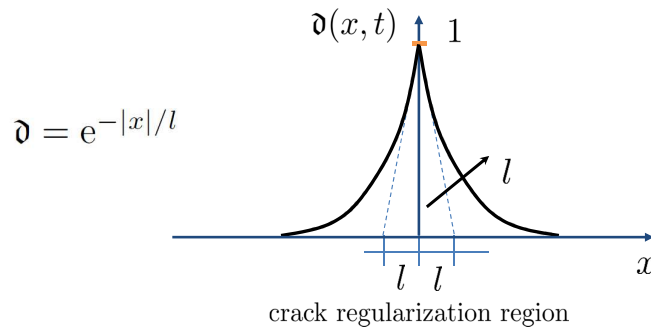


Fig. 3: Diffusive crack at regularization. 1D problem at $x = 0$ depending on the length scale parameter l .

According to (Miehe, Hofacker & Welschinger 2010), the equations associated with the phase field problem in the bulk take the form:

$$\vartheta - l^2 \Delta \vartheta = 0 \quad \text{in } \mathcal{B} \quad \text{and} \quad \nabla_{\mathbf{x}} \vartheta \cdot \mathbf{n} = 0 \quad \text{in } \partial\mathcal{B} \quad (2)$$

whereby $\Delta \vartheta$ is the Laplacian of the variable ϑ , and $\nabla_{\mathbf{x}} \vartheta$ stands for its spatial gradient.

The crack surface density functional $\gamma(\mathfrak{d}, \nabla_{\mathbf{x}}\mathfrak{d})$ accounting for the regularized crack topology is defined as:

$$\Gamma_c(\mathfrak{d}) := \int_{\mathcal{B}} \gamma(\mathfrak{d}, \nabla_{\mathbf{x}}\mathfrak{d}) \, d\Omega. \quad (3)$$

This functional endows the condition that Eq. (3) converges to the sharp crack surface Γ_c for the limit $l \rightarrow 0$ in the spirit of the Γ -convergence concept. The particular form of $\gamma(\mathfrak{d}, \nabla_{\mathbf{x}}\mathfrak{d})$ herewith adopted is in line with that previously defined in (Miehe, Hofacker & Welschinger 2010):

$$\gamma(\mathfrak{d}, \nabla_{\mathbf{x}}\mathfrak{d}) = \frac{1}{2l} \mathfrak{d}^2 + \frac{l}{2} |\nabla_{\mathbf{x}}\mathfrak{d}|^2. \quad (4)$$

Moreover, by the virtue of the introduction of the previous functional, the crack-related integral in the original Griffith formulation can be approximated by the volume integral as follows:

$$\int_{\Gamma_c} \mathcal{G}_c \, d\partial\Omega \approx \int_{\mathcal{B}} \mathcal{G}_c \gamma(\mathfrak{d}, \nabla_{\mathbf{x}}\mathfrak{d}) \, d\Omega, \quad (5)$$

Accordingly, the total energy functional of the solid reads (Fig. 4):

$$\Pi(\mathbf{u}, \mathfrak{d}) = \int_{\mathcal{B}} \psi(\boldsymbol{\varepsilon}, \mathfrak{d}) \, d\Omega + \int_{\mathcal{B}} \mathcal{G}_c \gamma(\mathfrak{d}, \nabla_{\mathbf{x}}\mathfrak{d}) \, d\Omega + \Pi_{ext}(\mathbf{u}) = \Pi_{int}(\mathbf{u}, \mathfrak{d}) + \Pi_{ext}(\mathbf{u}), \quad (6)$$

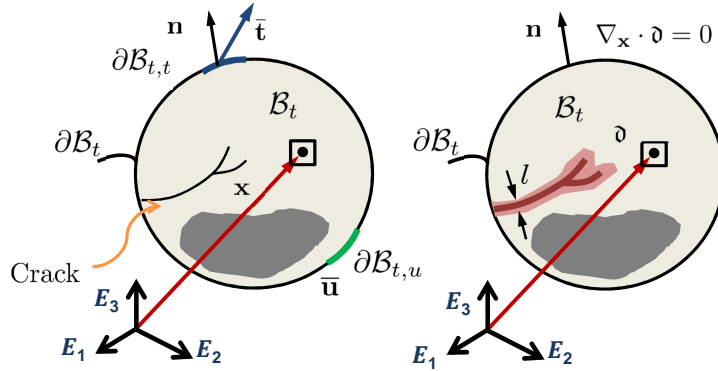


Fig. 4: Phase field method for diffusive crack modeling for bulk fracture: representation for arbitrary bodies. Left plot identifies an arbitrary cracked body using accounting for a discrete crack, whereas the right plot identifies the regularized crack representation using the phase field approach of fracture with the corresponding boundary condition.

where the first term represents the elastic energy that is affected by the degradation variable, and the second term stands for the dissipated energy due to the crack evolution characterized by the fracture toughness \mathcal{G}_c (both terms are arranged into the internal functional $\Pi_{int}(\mathbf{u}, \mathfrak{d})$); finally $\Pi_{ext}(\mathbf{u})$ accounts for the contribution of the external actions. Note that in the previous derivations, in a 2D setting, body and boundary integrals are associated with surface and line integrals, respectively. The corresponding extension to 3D analyses encompasses the evaluation of such terms volume domains and crack-surface regions, respectively.

One key aspect of this numerical technique is the fact that crack propagation results from the direct competition between the bulk and crack energy terms. The displacement and phase fields are then determined by minimizing the energy functional given in Eq. (6), which can be performed following either fully monolithic or a staggered solution schemes (Miehe, Hofacker & Welschinger 2010, Miehe, Welschinger & Hofacker 2010).

In order to prevent cracking in regions under compression states, the elastic energy term of the solid ($\psi(\boldsymbol{\varepsilon}, \mathfrak{d})$) admits the use of the spectral decomposition to split the traction and compression counterparts as follows (Miehe, Hofacker & Welschinger 2010):

$$\psi(\boldsymbol{\varepsilon}, \mathfrak{d}) = \mathfrak{g}(\mathfrak{d})\psi_+^e(\boldsymbol{\varepsilon}) + \psi_-^e(\boldsymbol{\varepsilon}), \quad (7a)$$

$$\psi_+^e(\boldsymbol{\varepsilon}) = \frac{\lambda}{2} (\langle \text{tr}[\boldsymbol{\varepsilon}] \rangle_+)^2 + \mu \text{tr}[\boldsymbol{\varepsilon}_+^2], \quad (7b)$$

$$\psi_-^e(\boldsymbol{\varepsilon}) = \frac{\lambda}{2} (\langle \text{tr}[\boldsymbol{\varepsilon}] \rangle_-)^2 + \mu \text{tr}[\boldsymbol{\varepsilon}_-^2], \quad (7c)$$

being λ y μ the Lamé constants; $\boldsymbol{\varepsilon}_+$ and $\boldsymbol{\varepsilon}_-$ respectively stand for the positive and negative parts of the infinitesimal strain tensor. The symbol $\text{tr}[\bullet]$ identifies the trace operator, whereas $\langle \bullet \rangle_{\pm}$ denotes the Macaulay bracket: $\langle \bullet \rangle_{\pm} = (\bullet \pm |\bullet|)/2$. Note that alternative schemes such as the isochoric-volumetric decomposition can be also adopted in a straightforward manner.

A possible choice of the degradation function $\mathfrak{g}(\mathfrak{d})$ reads

$$\mathfrak{g}(\mathfrak{d}) = (1 - \mathfrak{d})^2 + \mathcal{K}, \quad (8)$$

where \mathcal{K} is a residual stiffness parameter and its value is set equal to 0.0038.

Following standard thermodynamic arguments, the Cauchy stress tensor for the PF formulation can be expressed as:

$$\boldsymbol{\sigma} := \frac{\partial \hat{\psi}}{\partial \boldsymbol{\varepsilon}} = \mathfrak{g}(\mathfrak{d})\boldsymbol{\sigma}_+ + \boldsymbol{\sigma}_-; \quad \text{with } \boldsymbol{\sigma}_{\pm} = \lambda (\langle \text{tr}[\boldsymbol{\varepsilon}] \rangle_{\pm}) \mathbf{1} + 2\mu \boldsymbol{\varepsilon}_{\pm}, \quad (9)$$

being $\mathbf{1}$ second order identity matrix, and $\boldsymbol{\sigma}_{\pm}$ denoting the positive and negative parts of $\boldsymbol{\sigma}$. Note that alternative positive-negative decomposition schemes such as that proposed in (Steinke & Kaliske 2018) and (Strobl & Seelig 2015) can be adopted in the current modeling framework in a simple manner. However, the discussion of the performance of such alternative decomposition methods are beyond the scope of the present study. In addition, in the current formulation, we account for the irreversible character of fracture processes via an history dependent variable in line with (Miehe, Hofacker & Welschinger 2010). In order to perform a careful analysis regarding possible effects of the proposed model to ensure such irreversibility, the procedure proposed in (Linse, Hennig, Kstner & de Borst 2017) is a plausible way to overcome some potential drawbacks preserving the accuracy of the method.

The numerical implementation of this PF formulation for damage into the bulk is given in Appendix A.

2.2 Coupling between the phase field approach of fracture and interface cohesive zone formulations for heterogeneous media

The development of a numerical framework in the spirit of the phase field approach applicable to composite materials is a timely research area which is still quite unexplored. Most of the existing works usually take into consideration bi-material layers or particle-reinforced materials, but they do not tackle the potential decohesion events that can take place at the interfaces between components.

Originally, in order to capture complex delamination path in heterogeneous media, Paggi and Reinoso proposed a numerical technique in (Paggi & Reinoso 2017), which consistently combines the PF approach in the bulk with interface elements complying with the cohesive zone concept. This new paradigm has been successfully applied at the macro-scale for poly-crystalline materials (Paggi, Corrado & Reinoso 2018), shell-like structures and layer-based ceramics (Carollo et al. 2017, Carollo et al. 2018) This new approach is also suitable for capturing fracture processes at different scales and therefore it is applicable to micromechanical analysis of fiber-reinforced composites.

In this setting, the basic hypothesis of such a technique relies on the consideration of a system which contains a crack Γ_b and a prescribed discontinuity Γ_i (characterizing the presence of an interface), whereby a generic point of the interface is denoted by the position vector \mathbf{x}_c , see Fig. 5.

Accordingly, the dissipative phenomena in the system can potentially arise from two different sources: (i) the crack propagation within the bulk, and (ii) the delamination events along the existing interfaces.

Assuming this scenario, the total potential energy given in Eq. (6) is herewith recalled. In particular, the current methodology assumes that the dissipative term in Eq. (6) can be additively decomposed

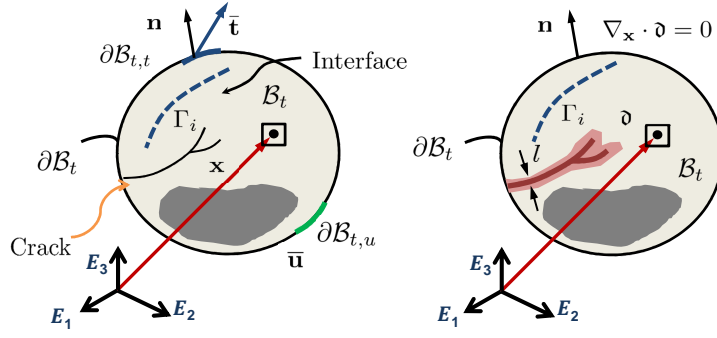


Fig. 5: PF-CZ method for diffusive crack modeling for heterogeneous media. The dashed line corresponds to the placement of prescribed interfaces in the system. Left and right plots identify the sharp and smeared crack representations in the bulk.

into: (i) the energy dissipated in the bulk, which is triggered following the standard PF approach and (ii) the energy dissipated via delamination along the existing interfaces, complying with a cohesive-like representation. This split is envisaged via the consideration of the bulk and the interface fracture energies, which are denoted by \mathcal{G}_c^b and \mathcal{G}^i , respectively.

In line with this assumption, the internal body functional renders

$$\Pi_{int}(\mathbf{u}, \Gamma_b, \Gamma_i) = \Pi_B + \Pi_{\Gamma_b} + \Pi_{\Gamma_i} = \int_{B \setminus \Gamma} \psi^e(\boldsymbol{\varepsilon}) d\Omega + \int_{\Gamma_b} \mathcal{G}_c^b(\mathbf{u}, \mathfrak{d}) d\Gamma + \int_{\Gamma_i} \mathcal{G}^i(\mathbf{g}, \mathfrak{h}, \mathfrak{d}) d\Gamma, \quad (10)$$

being \mathbf{g} the continuous displacement between the two flanks of the interface, whilst \mathfrak{h} and \mathfrak{d} denote an history variable associated with the interface degradation upon failure (Verhoosel & de Borst 2013) and phase field variable in the bulk, respectively.

Without loss of generality, a tension cut-off interface behavior is henceforth adopted. The coupling with the phase field in the bulk is accomplished by modifying the critical displacement gap for each fracture mode through the following relationship (Paggi & Reinoso 2017): $g_c(\mathfrak{d}) = (1 - \mathfrak{d})g_{c,0} + \mathfrak{d}g_{c,1}$, where $g_{c,0} = g_c(\mathfrak{d} = 0)$ and $g_{c,1} = g_c(\mathfrak{d} = 1)$. Note however that, the current formulation preserves the energy that is released along the interface.

The corresponding traction-displacement gap law for fracture Modes I and II are given by (Fig. 6):

$$\sigma = \begin{cases} k_n \frac{g_n}{g_{nc}}, & \text{if } 0 < \frac{g_n}{g_{nc}} < 1; \\ 0, & \text{if } \frac{g_n}{g_{nc}} \geq 1, \end{cases} \quad \tau = \begin{cases} k_t \frac{g_t}{g_{tc}}, & \text{if } 0 < \frac{g_t}{g_{tc}} < 1; \\ 0, & \text{if } \frac{g_t}{g_{tc}} \geq 1. \end{cases} \quad \text{where } \sigma \text{ and } \tau \text{ identify the in-} \quad (11) \quad (12)$$

terface tractions associated with fracture Modes I and II, respectively, whereas g_n and g_t denote the normal and tangential gaps.

Then, the apparent interface stiffness k (see (Paggi & Reinoso 2017) for a more thorough discussion about the attributes of the present interface law) can be related to the damage state at the surrounding bulk region via the phase field variable \mathfrak{d} . The specific form of the k_n and k_t are given by

$$k_n = k_{n,0} \left(\frac{g_{nc,0}}{g_{nc}} \right)^2; \quad k_t = k_{t,0} \left(\frac{g_{tc,0}}{g_{tc}} \right)^2, \quad (13)$$

where k_0 and g_0 indicate the initial normal and tangential stiffness for intact surrounding bulk, respectively, being the corresponding critical gaps $g_{nc,0}$ and $g_{tc,0}$.

Interface failure is triggered using a standard quadratic fracture criterion:

$$\left(\frac{\mathcal{G}_I^i}{\mathcal{G}_{IC}^i} \right)^2 + \left(\frac{\mathcal{G}_{II}^i}{\mathcal{G}_{IC}^i} \right)^2 = 1, \quad (14)$$

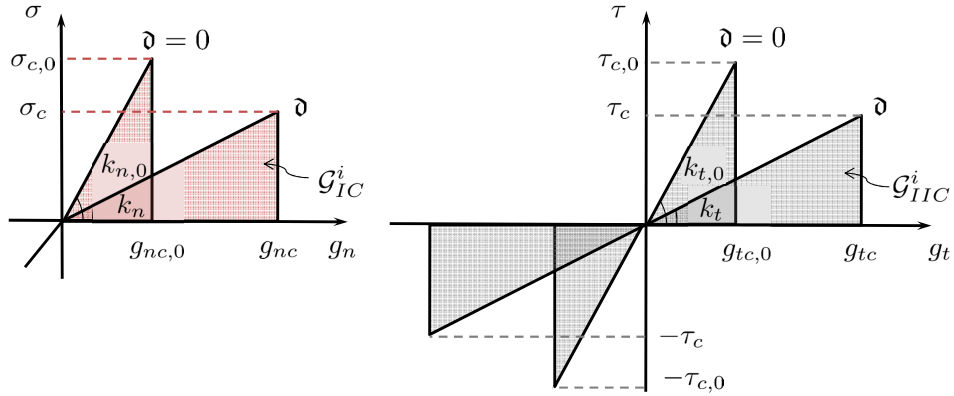


Fig. 6: Schematic representation of the traction separation law of the CZM which accounts for the PF variable. Left: Mode I CZM traction σ vs. g_n . Right: Mode II CZM traction τ vs. g_t .

denoting \mathcal{G}_I^i and \mathcal{G}_{II}^i the energy release rates associated with the fracture Modes I and II:

$$\mathcal{G}_I^i(\mathfrak{d}) = \frac{1}{2}k_{n,0}g_n^2 \frac{g_{nc,0}^2}{[(1-\mathfrak{d})g_{nc,0} + \mathfrak{d}g_{nc,1}]^2}; \quad \mathcal{G}_{II}^i(\mathfrak{d}) = \frac{1}{2}k_{t,0}g_t^2 \frac{g_{tc,0}^2}{[(1-\mathfrak{d})g_{tc,0} + \mathfrak{d}g_{tc,1}]^2}. \quad (15)$$

The corresponding critical energy release rates in the present model, identified by \mathcal{G}_{IC}^i \mathcal{G}_{IIC}^i , render

$$\mathcal{G}_{IC}^i = \frac{1}{2}g_{nc,0}^2k_{n,0}; \quad \mathcal{G}_{IIC}^i = \frac{1}{2}g_{tc,0}^2k_{t,0}. \quad (16)$$

Finally, it is worth mentioning that the present interface response can be extended to 3D and large deformation setting in a straightforward manner, see (Carollo et al. 2017).

3 Representative applications

This section deals with the assessment of the current modeling strategy for triggering damage events in fiber-reinforced composites from a micromechanical standpoint. Therefore, the constituents are defined according to their respective mechanical and fracture properties.

One of the key aspects of the computational strategy is the direct competition between fiber-matrix debonding along the existing interface and the matrix failure in a consistent manner. Additionally, the parameters, which characterize the system response and are inserted as input data, are physically-sound. Moreover, one additional attribute is the fact that the combined PF-CZM approach allows fracture evolution to be triggered without the user intervention throughout the simulation and excluding the consideration of an initial crack or defect that nucleates the subsequent progression.

In the sequel, we present numerical results concerning the onset and growth of cracks in different cases comprising: (i) single-fiber failure problem subjected to different loading cases and (ii) two-fibers problem, whereby the effect of the inter-fiber spacing and the angle between the load direction and the fibers alignment are analyzed.

Within the scope of the current investigation, simulations herewith presented are restricted to the case of plane strain conditions.

3.1 Single fiber-matrix decohesion problem

The first application illustrates the prediction of crack initiation and evolution in fiber-reinforced composite materials from a micromechanical perspective, concerning a single fiber-matrix decohesion problem. This application has received a huge attention in the scientific community in the last two decades, see (García et al. 2014, Bourdin et al. 2000, Távora et al. 2011) and the references therein given. As discussed above, the main capability of the proposed numerical framework is the fact that a direct competition

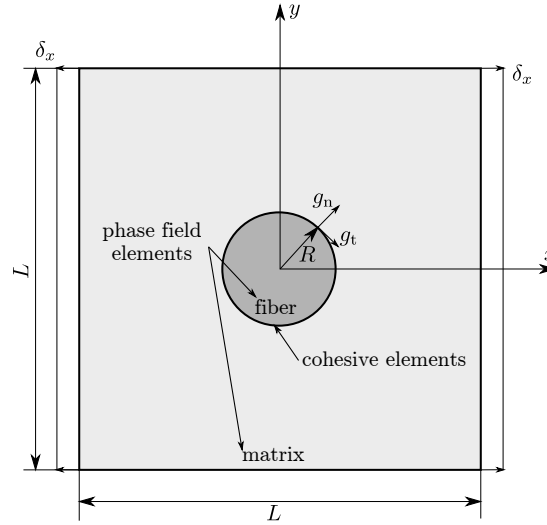


Fig. 7: Micromechanics of fiber-reinforced composite materials under transverse tensile loading conditions: geometry and boundary conditions.

between fiber-matrix debonding along the existing interface and matrix failure are concurrently simulated throughout the numerical analysis.

The system under analysis is defined by: (i) a single fiber with circular transverse section with radius $R = 0.0125$ mm, (ii) a surrounding squared-matrix domain with side length equal to $L = 0.2$ mm, and (iii) an interface that is located between the previous entities. In line with (García et al. 2014), both matrix and fiber are taken as linear elastic materials, and initially the fiber-matrix interface is assumed as perfectly bonded. **Note that L is large enough relatively to R in order to neglect the edge effects.**

The material properties corresponding to the fiber and matrix and the interface fracture properties are collected in Table 1, see (Correa et al. 2008, Arteiro et al. 2014). According to the tension cut-off interface behavior previously detailed, the apparent stiffness properties of the interface, i.e. k_{n0} and k_{t0} prior damage initiation, can be computed in a straightforward manner. Through the exploitation of the symmetry of the system, only one quarter of the domain is initially considered.

Material	E [GPa]	ν	\mathcal{G}_C [N/mm]	l [mm]	Interface Property	σ_C [MPa]	\mathcal{G}_C [N/mm]
Fiber	201	0.22	16	0.39	Fracture Mode I	75	0.002
Matrix	2.8	0.33	0.016	0.0009	Fracture Mode II	90	0.008

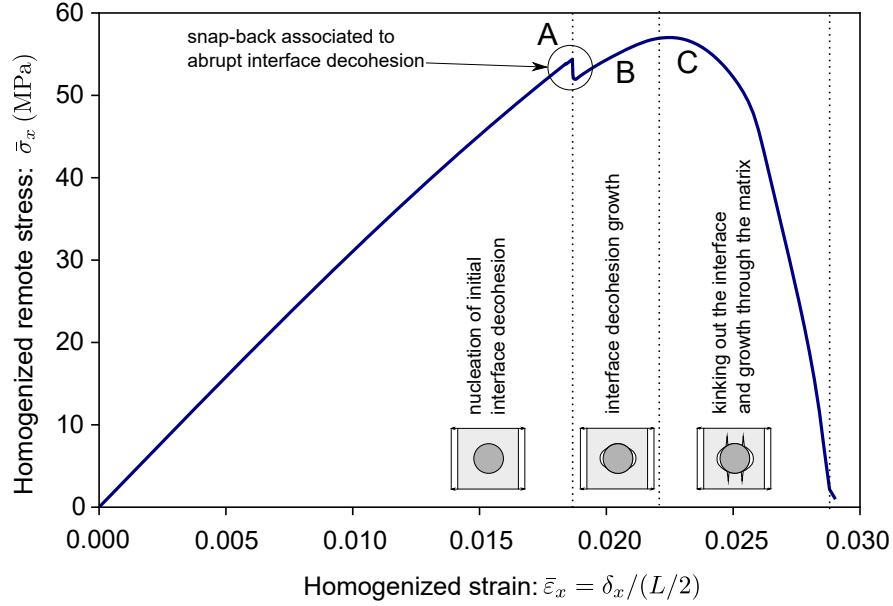
Table 1: Mechanical properties of fiber, matrix and interface.

For the application of the PF-CZM approach, the domain is discretized using first-order isoparametric elements. The mesh characteristics are: 30274 elements for the matrix, 1200 elements for the interface and 19095 for the fiber. In the sequel, different loading cases are presented.

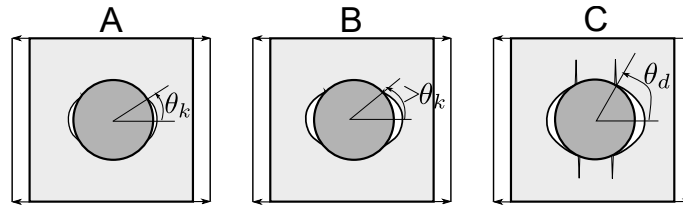
3.1.1 Transverse tensile loading conditions: benchmark case

The first case under study concerns the response of the system subjected to transverse tensile loading conditions. The simulations are conducted under displacement control at the lateral edges of the system (Fig. 7), δ_x denoting the external displacement from which the imposed apparent strain can be computed as $\tilde{\varepsilon}_x = \delta_x/(L/2)$. The average stress is computed by adding all the nodal reaction forces on the right edge and dividing by the edge length. At upper and lower edges free-stress boundary conditions are prescribed.

Fig. 8 depicts the load-displacement evolution curve of the current analysis. The response of the system is characterized by four different stages:



(a)



(b)

Fig. 8: Micromechanics of fiber-reinforced composite materials under transverse tensile loading conditions: (a) stress-strain evolution curve and damage pattern at different stages of the simulation. (b) Debonding and kinking angles.

- The first stage of the response shows a linear elastic evolution. In this stage the nonlinearities introduced by (i) the initiation of the cohesive separation between fiber and matrix along the interface and (ii) the phase field at fiber and matrix do not play any role in the global mechanical behavior of the system. This stage concludes with the sudden decohesion of a finite part of the fiber-matrix interface. This sudden decohesion is reflected in a drop of the stress-strain curve, see Fig. 8. This failure is abrupt due to the fact that the interface crack is initiated at a non-singular point, generating a snap-back instability. ~~Actually, to obtain a snap back instability in the equilibrium path, a different solution scheme should be used, as arc-length. However, the behavior observed here is what typically is obtained using a Newton-Raphson scheme if a snap-back instability is in the system. The influence of the element size and time step on the snap-back observed was studied and the equilibrium path tends to a fixed path for element size and time size small enough.~~
- The second stage is characterized by the growth of fiber-matrix decohesion along the interface, in agreement with (Mantič 2009, García et al. 2014, Távora et al. 2011). This failure is estimated to progress up to an angle approximately equal to 56° . As was mentioned above, this stage is unstable so that the interface crack growth is triggered between two consecutive pseudo-time steps in the simulations. The current predictions contrast with those given in (Bourdin et al. 2000), whereby the lack of the interface consideration leads to the prediction of matrix failure very close to the interface.
- A further increase in the applied displacement leads to the third stage of the system evolution, which features further interface decohesion followed by kinking of the crack into the matrix. This is a typical response in the fracture between dissimilar materials, when an existing interface crack tends to kink out into (preferentially) the compliant material (in this case the matrix) due to the higher crack

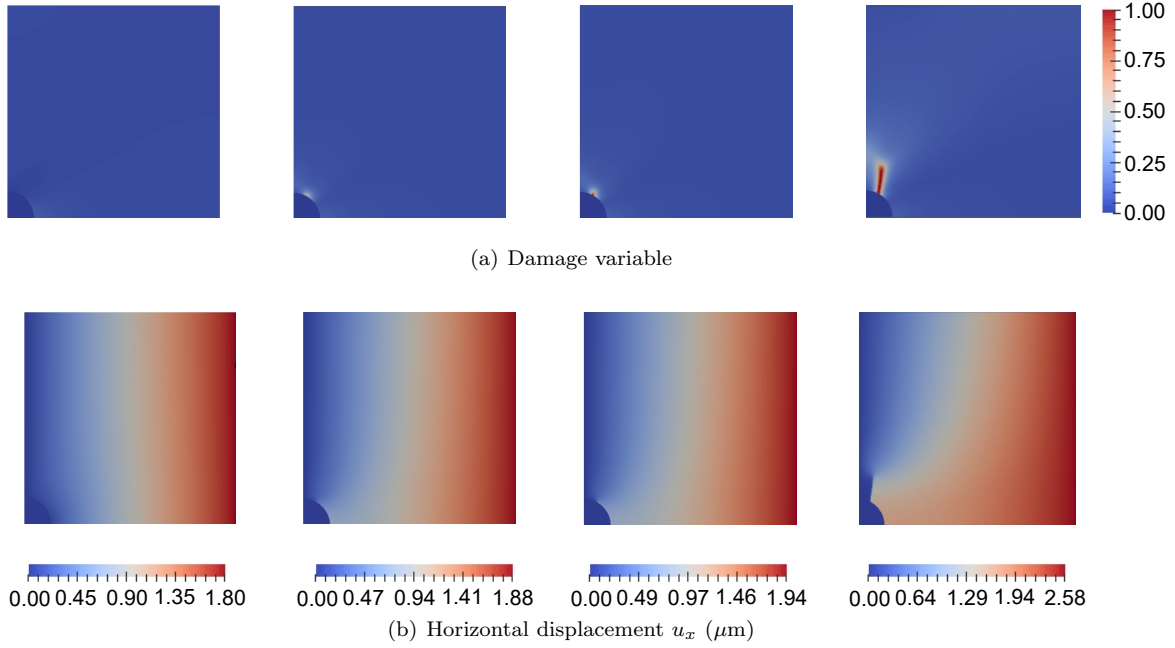


Fig. 9: Micromechanics of fiber-reinforced composite materials under transverse tensile loading conditions: (a) Damage pattern. (b) Contour plot of the horizontal displacement field.

growth resistance along the interface. In this particular case this tendency is promoted by the fact that the fracture mixity of the interface crack grows with the decohesion angle. These results generate an increase of the fracture toughness at the crack tip for decohesion, making energetically more favourable crack growth into the matrix. In the present simulations, interface progression failure is estimated to progress from 56° to 60° . After this, the crack kinks out and penetrates into the matrix. These predictions are in excellent agreement with the observations in (Correa et al. 2008). From a qualitative point of view, this stage exhibits a continuous increasing stress-strain evolution along the loading path upon complete failure.

- Finally, the crack progresses along the matrix, which is reflected by a decrease in the load carrying capacity in the averaged stress-strain curve. In this case (single fiber) the crack progresses without any restriction up to reaching the domain boundary. For interacting fibers, the behavior will be more complex and it will be examined in Section. 3.2.

It is worth mentioning that the four stages previously described are in agreement with those identified in (Correa et al. 2008, Legarth & Yang 2016). To illustrate such a crack evolution, the damage pattern and the horizontal displacement field at the different stages during the simulations are shown in Fig. 9. The discontinuity in the displacement field identifies the separation associated with the crack and the progress of failure. In this graph, both micromechanical failure modes, i.e. interface decohesion and matrix cracking, can be clearly identified.

Finally, during the first and the second stage it is remarkable to note that no damage is found in the matrix, see the first two columns in Fig. 9. At these stages, damage is localized in the interface decohesion process. Once the abrupt decohesion is produced, a crack begins to nucleate in the matrix around the interface crack tip. This fact is clearly observable the third column of Fig. 9. This point of nucleation will be the origin of the crack progressing into the matrix, see fourth column in Fig. 9.

3.1.2 Symmetry in the crack pattern

The initial geometry and loading conditions of the problem (Fig. 7) present two axes of symmetry. According to that, it could be argued that the failure progression should be symmetric with respect to these two axes. In view of the numerical results presented in the previous section, the symmetric solution in this problem corresponds to the onset of two separated decohesion zones at the fiber-matrix interface,

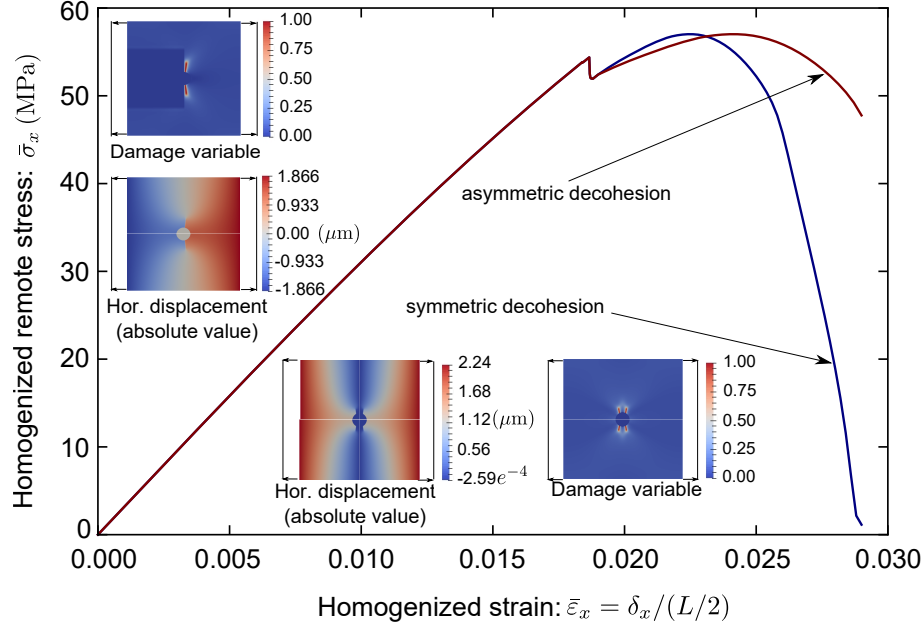


Fig. 10: Micromechanics of fiber- reinforced composite materials under transverse tensile loading conditions: one or two debonds.

symmetric with respect to the y -axis. However, this is not in line with the experimental evidences as discussed in (García, Mantič & Graciani 2015) that corresponded to a single (asymmetric) fiber-matrix interface debonding. The reason for that emerges from the condition stating that it is the set of solutions which should fulfill the symmetry conditions and not necessarily each of them. In those problems where only one solution is possible, the direct consequence is that this unique solution is symmetric, e.g. the problems of the Linear Theory of Elasticity. However, in this case the solution is not necessarily unique and the symmetric set of solutions is composed by three different options:

- An asymmetric decohesion on the right side of the fiber-matrix interface.
- An asymmetric decohesion on the left side of the fiber-matrix interface.
- A symmetric decohesion on the right and left side of the fiber-matrix interface.

According to (García et al. 2015), the coupled criterion of Finite Fracture Mechanics (FFM) predicts an asymmetric debond, as observed in the experiments. In that investigation, the authors rigorously analyzed the set of the solutions mentioned above in a separate manner, obtaining that the asymmetric solutions are preferential over the symmetric option. The physical justification for this behavior is attributed to the fact that a symmetric solution with two interface cracks would produce a shielding effect between the two cracks, and as a consequence a decreasing ability of releasing elastic energy per unit of newly formed cracked area. Thus, from an energetic point of view, the asymmetric solution is prevailing over the symmetric case.

The comparison between the current PF-CZ methodology and the coupled criterion is herein carried out by studying the different failure scenarios aforementioned and obtaining the corresponding critical loadings. This is possible because the coupled criterion requires the prescription of a geometry for the situation after the occurrence of the damage event. However, the numerical strategy herewith envisaged does not require any assumption associated with the qualitative form of the solution. In such a case, if instead of a quarter of the cell (previously performed) a half of the domain (upper one) is simulated, the symmetric solution with two interface cracks is obtained. The reason is that this is the equilibrium solution detected by the solution algorithm used. In order to promote the asymmetric solution for the comparison purposes, a higher fracture toughness is prescribed in one side of the fiber-matrix interface, acting as perturbation of the symmetric problem.

Fig. 3.1.2 shows the comparison of the stress-strain curves for the asymmetric and symmetric solutions along with the damage patterns through the proposed technique. It should be expected a bigger difference

between both critical stresses knowing that the asymmetric case has bigger interface fracture toughness. The justification for this discrepancy is the shielding effect between the two cracks in the symmetric case.

The physical justification for this behavior is attributed to the fact that a symmetric solution with two interface cracks would produce a shielding effect between the two cracks, and as a consequence a decreasing ability of releasing elastic energy per unit of newly formed cracked area. Thus, from an energetic point of view, the asymmetric solution is prevailing over the symmetric case.

An additional discrepancy between the symmetric and asymmetric solutions is the fact that both solutions lead to different predictions regarding the debonding and kinking angles. In this case, the current method predicts a lower kinking angle for the asymmetric case with respect to that corresponding to the two-debonds scenario. As the kinking angle decreases, the extension of the crack propagation into the matrix increases, because the crack is more far apart from the less resistant ligament. However, the snap-back in the evolution response is predicted to occur at the same stress and strain levels in both cases. In light of this discussion, it can be concluded that for the prediction of limit loads, the symmetric solution (and the study of a quarter of the domain) can be considered as a solution with an acceptable level of accuracy.

debonds number	θ_d [°]	θ_k [°]
1	58	74
2	56	60

Table 2: Asymmetric and symmetric case: debonding and kinking angles.

3.1.3 Size effect of the fiber radius

Size effect is a phenomenon inherently associated with fracture and damage mechanics, see (Bažant 2005). The PF approach for bulk fracture has shown to be able to predict the size effect accordingly to experimental observations, see (Reinoso, Arteiro, Paggi & Camanho 2017). For this problem, a size effect of the fiber radius has been reported (García et al. 2014). In order to evaluate the suitability of the present model to simulate the micromechanics of failure in composites, the ability to predict accurately the well-known size effect is herewith examined.

In this concern, the size effect is evaluated here by scaling the whole domain and fiber radius by using the same scaling factor in order to keep the volumetric fraction unchanged. The value of the final imposed displacement imposed is also multiplied by the same factor. Finally the results are compared in terms of homogenized (average) stress-strain curves, so the differences are only attributable to the presence of size effect.

Fig. 11 presents the stress-strain curves for several values of the fiber radius. The more remarkable difference is that smaller fibers have significantly higher critical stress. Moreover, this difference is even higher if the maximum stress is compared. For larger fibers, the stress-strain curves seem to tend to the same stress-strain curve. The explanation for this different size effect is that the failure behavior for larger fibers is governed by stress considerations, whereas for small fibers the failure behavior is controlled by energy considerations. Since the stress distribution is independent of the scale, the size effect is inhibited for large fibers, see (García et al. 2014) for a detailed discussion.

Another clear difference is that the behavior is much more brittle when the fibers have a larger radius. This is reflected in the stress-strain curves after the peak corresponding to the onset of debonding. It can be observed a significant increase in the difference between the stress of debond onset and the maximum stress for small fibers. Furthermore, the energy dissipation is much higher for small fibers, which shows a tougher situation. In addition, failure of small fibers is observed for higher strain values. Thus, small fibers corresponds to scenarios whereby larger energy dissipation is required (which can be also denominated as *pseudo-ductile character*).

Fig. 12 shows the comparison of the size effect predicted by the present model with the predictions of the coupled criterion of the Finite Fracture Mechanics (FFM). This criterion assumes a crack onset occurs (a decohesion in this problem) when the next two conditions are fulfilled simultaneously: i) the stresses along the potential crack path exceed the strength and ii) the crack onset is energetically admissible. The FFM model used here for the sake of comparison is similar to the FEM model shown in fig:Micro a

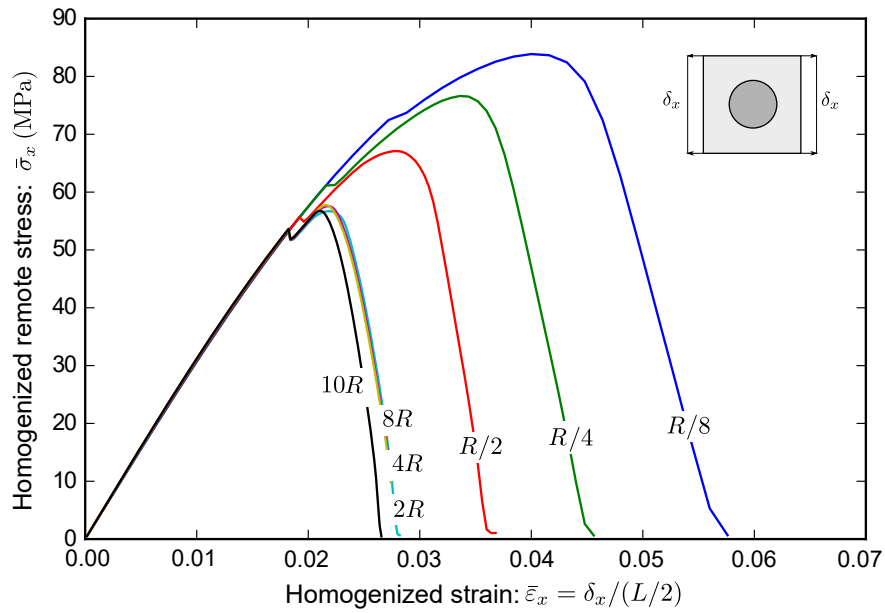


Fig. 11: Micromechanics of fiber- reinforced composite materials under transverse tensile loading conditions: fiber size effect.

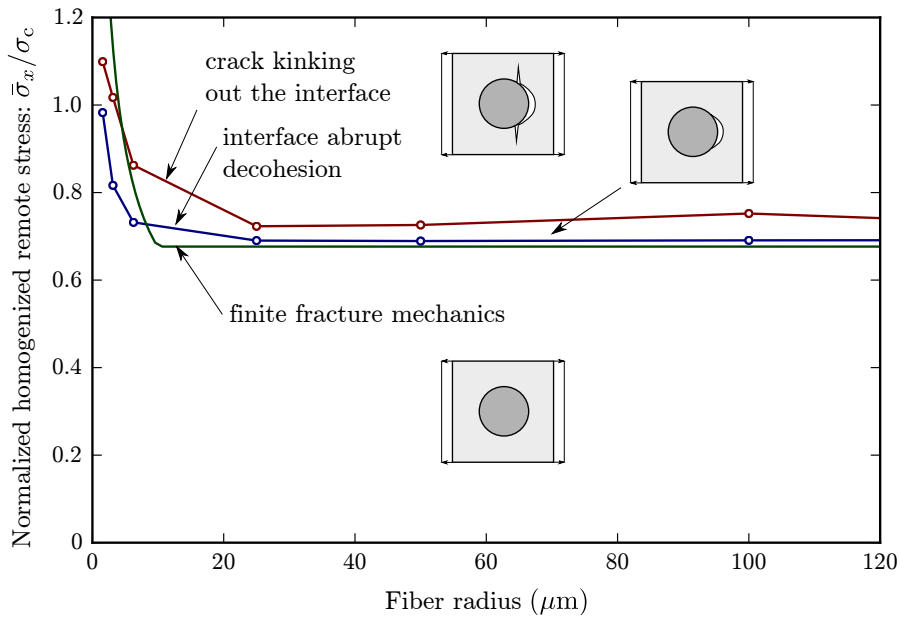


Fig. 12: Micromechanics of fiber- reinforced composite materials under transverse tensile loading conditions: fiber size effect and comparison between the present PF-CZM predictions and those provided by finite fracture mechanics.

circular inclusion surrounded by a very large square of matrix subjected to a uniaxial tension. The stress leading to the debond onset is represented along with the stress for which the crack kinks out the interface. The critical stress for the debond onset predicted by the finite fracture mechanics is also plotted. In this graph, a good agreement can be observed between the current PF-CZM and FFM from both qualitative and quantitative points of view. In particular, from a qualitative perspective, a clear change of tendency is observed around $R = 10 \mu\text{m}$, going from a strong size effect for smaller fibers to a total independence for larger fibers. Finally, at quantitative level, the predictions of the two models are very similar to each other.

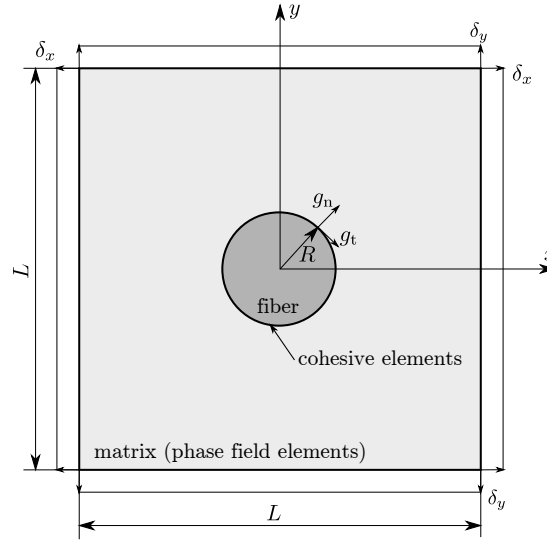


Fig. 13: Micromechanics of fiber-reinforced composite materials under biaxial tensile loading conditions: geometry and boundary conditions.

3.1.4 Effect of the secondary transverse loading on the inter-fiber failure

The analysis of the current inter-fiber failure problem for the single fiber domain is also extended by adding secondary transverse loading. The presence of the secondary stress can notably affect the failure onset and evolution of the present problem. For this purpose, the external loading conditions applied to the system are accordingly modified including a secondary stress σ_y , see Fig. 13. The nomenclature henceforth adopted follows the scheme: $\delta_y = n\delta_x$, then for instance the case $n = 1$ ($\delta_x = \delta_y$) yields to a biaxial tensile state along both perpendicular directions. Note that any plain remote stress state can be reduced to a pair of normal stresses along two perpendicular directions, so the results obtained here covers any remote stress state, even including shear stresses.

The corresponding stress-strain evolution curves for the x -direction associated with the current representative scenarios are depicted in Fig. 14. From this plot, it can be observed that the load level required for the initiation of growth is greater for larger values of σ_y . The reason is that a secondary tensile stress generates a compression at the interface points where decohesion takes place due to the different contraction due to Poisson effect of fiber and matrix. Thus, since matrix is more compliant than the fiber, the matrix tends to contract more in the x -direction due to the tensile stress state along the y -direction, producing a compression at the interface points. This compression counteracts the tensile state produced by the main transverse load, making more difficult the onset of decohesion. On the other hand, a secondary compression has the contrary effect, it makes easier the onset of debonding.

In addition, it can be observed in Fig. 14 that the presence of a secondary stress also modifies qualitatively the behavior. A secondary tensile stress produces a much more brittle behavior. In fact, in the limit for a biaxial tensile state ($n = 1$), the failure is totally brittle: an abrupt debond onset occurs spanning the whole fiber-matrix interface. **After the total decohesion of the interface, the stresses increase at the matrix, producing the instantenous failure of the whole matrix domain.** In contrast, a much more *pseudo-ductile* and tough behavior is found when the compression is relatively significant. For example, for $n = -1$, the stress-strain curve shows a wide range of strain where the debond is slowly growing along the fiber-matrix interface, the critical strain at failure being almost ten times larger than for $n = 1$.

Fig. 15 represents the critical remote stresses (σ_x, σ_y) predicted for the onset of debonding and crack kinking out of the interface. This plot clearly illustrates the effect of the secondary transverse load. This prediction is in agreement with other previous models (Távora et al. 2016, Mantič & García 2012).

With regard to failure initiation, the location of the interface debonding coincides with that corresponding to the uniaxial tensile case for low values of the secondary transverse load. As for the unstable fiber-matrix debonding, current simulations estimate lower angles θ_d as the secondary loading increases,

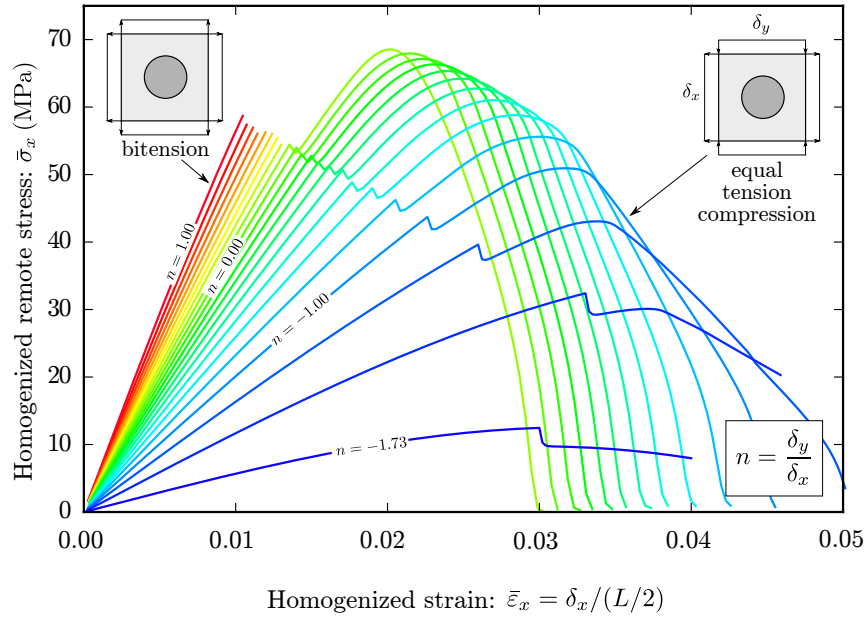


Fig. 14: Micromechanics of fiber- reinforced composite materials under biaxial transverse tensile loading conditions: homogenized stress-strain curves.

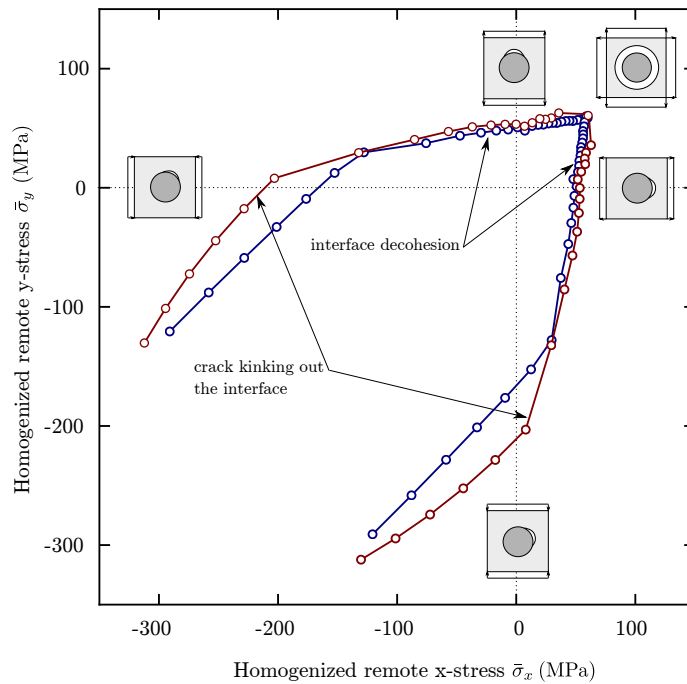


Fig. 15: Micromechanics of fiber- reinforced composite materials under biaxial transverse tensile loading conditions: Critical remote stresses for interface decohesion or for crack kinking out of the interface.

being this result in line with (Correa, París & Mantič 2013). When the secondary load becomes more significant, the debond location moves through the interface points more loaded, see Fig. 15.

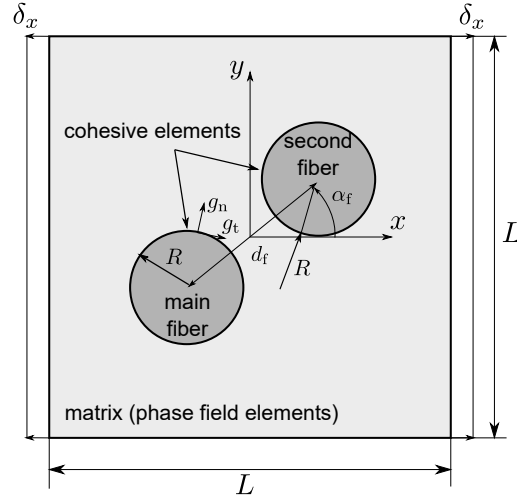


Fig. 16: Two-fibers model: geometry and boundary conditions.

3.2 Two fiber-matrix decohesion problem

In this section, the importance of the presence of neighbouring fibers with regard to the micromechanical failure characteristics in composites is examined. This effect provides a more profound understanding of the fracture processes in fibrous composite materials. The present analysis is restricted to the uniaxial tensile loading as depicted in Fig. 16. However, additional cases can be assessed without remarkable limitations.

The model comprises a main fiber and a secondary fiber, whose position is modified in order to explore different cases. In the current study, complying with standard fiber volume fraction for hexagonal packing, the initial distance between both fibers is set equal to following values: $d_f = [2.116R, 2.6R, 3R]$, where $R=0.0125$ mm stands for the fiber radius. Initially, the angle between the fibers α_f is equal to 45° .

The stress-strain evolution curve of the system is depicted in Fig. 17 for different values of the distance between the fibers but keeping unchanged the relative angle between them. This graph evidences that a quasi-identical initial linear elastic phase of the response can be observed for the chosen distance values. Furthermore, the evolution curves display a first sudden drop which is associated with the unstable debonding event of the secondary fiber. Note that this point is slightly affected by the inter-fiber distance, obtaining higher values as d_f increases.

After that, the second stage of the evolution is characterized by the stable fiber-matrix debonding of the secondary fiber. This second stage concludes when the unstable interface decohesion in the central fiber occurs, being characterized in the stress-strain evolution by a second drop. Again, this second debonding takes place at higher load levels for increasing d_f values.

Progressing on the loading path, the third phase comprises the stable interface failure of the central fiber till this crack tends to kink out towards the matrix. During the simulations, it is observed that this kinking progresses till reaching the secondary fiber interface crack. After this, subsequent kinks of interface cracks at the central and secondary fibers towards the matrix take place. The final phase of the present response features a notable stiffness degradation for each of the cases under consideration upon complete failure, whereby the larger d_f is set, the higher maximum load value is obtained.

It is worth mentioning that differing from alternative approaches (Zhuang, Talreja & Varna 2018), the current methodology endows a robust and reliable competition of the different failure mechanisms throughout the simulation and without the user intervention.

The effect of the position of the secondary fiber with respect to the central one is also studied. Fixing the distance between the fibers equal to $d_f = 2.116R$, the following secondary fiber angles $\alpha_f = [30^\circ, 45^\circ, 60^\circ]$ are studied. The obtained predictions are displayed in Fig. 18. From this graph, it can be observed that, there exist two drops on the stress-strain evolution curve in the case of 45° . Conversely, for the remaining cases, only one drop along the evolution which corresponds with the unstable debonding

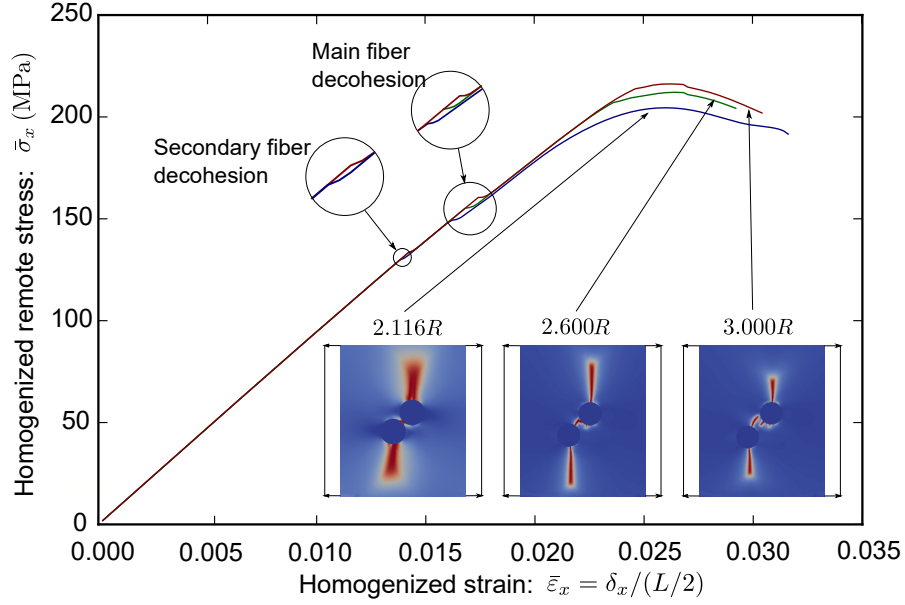


Fig. 17: Micromechanics of two fibers- reinforced composite materials under transverse tensile loading conditions: Influence of the distance between fibers on the stress-strain evolution curve.

of the main fiber is predicted. From the quantitative perspective, it can be also deduced that for configurations with an individual instability in the evolution, the interface crack onset requires higher load levels as the angle decreases. However, in the case of configurations with two instabilities, the highest snap-back load is found.

It can be observed that the debonding and kinking angles are predicted to increase for higher angles between fibers, see Tab. 3. The only exception is the debonding angle of the main fiber for the 45° case, because is the smallest one due to the presence of a previous instability.

$\alpha_f [^\circ]$	$\theta_{d,SF} [^\circ]$	$\theta_{d,MF} [^\circ]$	$\theta_k [^\circ]$
30	NO	51	113
45	90	39	118
60	NO	76	135

Table 3: Two fibers problem: Influence of the distance between fibers on the debonding and kinking angles.

$d_f [\text{mm}]$	$\theta_{d,SF} [^\circ]$	$\theta_{d,MF} [^\circ]$	$\theta_k [^\circ]$
$2.116R$	90	39	118
$2.6R$	102	47	142
$3R$	112	51	151

Table 4: Two fibers problem: Influence of the distance between fibers on the debonding and kinking angles.

4 Concluding remarks

The results presented here shows that the approach combining the phase approach for fracture and cohesive zone model elements is a very useful tool to study failure initiation in composites at the microscale. The approach is able to predict all the stages of the failure process and its versatility allows studying

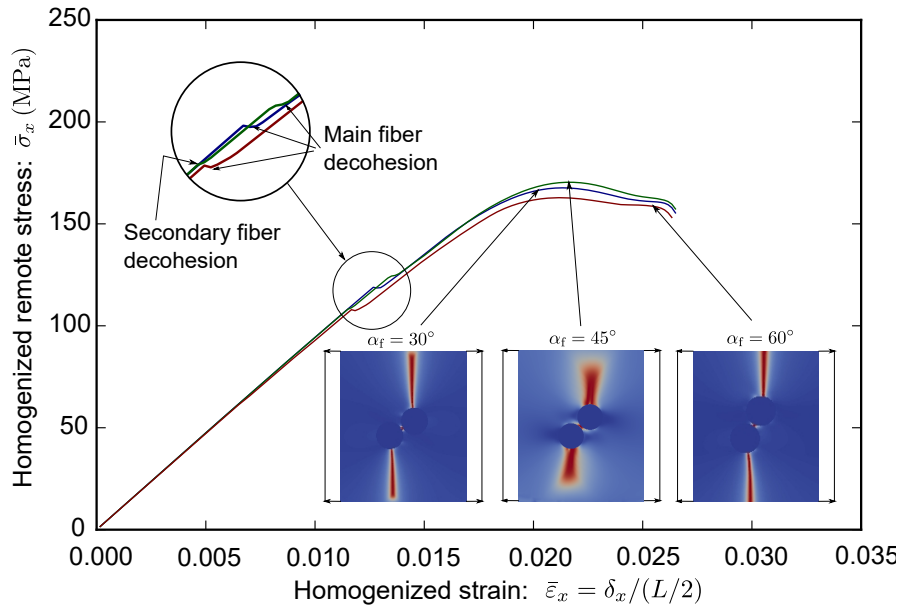


Fig. 18: Micromechanics of two fibers- reinforced composite materials under transverse tensile loading conditions: Influence of the angle between fibers on the stress-strain evolution curve.

the effect of the problem parameters on the failure process. The predictions obtained here agree with the majority of results presented in the literature during the last few decades, being the advantage that all the results have been obtained in the present setting by a single robust computational approach without requiring semi-analytical solutions or approximations on the initial stress states.

The stages of the process of failure initiation in composites under **transverse** load have been studied, obtaining an agreement with experiments: firstly a decohesion nucleates at the most loaded region of the fiber-matrix interface. For a certain critical remote transverse load, an abrupt decohesion occurs leading to a crack in the fiber-matrix interface. This crack grows along the interface and subsequently kinks out the interface through the matrix. **Finally**, the crack grows through the matrix.

The approach used here is also able to predict a strong size effect of the fiber radius, already reported in other works and especially in the studies based on finite fracture mechanics. For small fibers, the critical stress for the abrupt onset increases. In addition, the failure behavior is much tougher and more ductile for small fibers than for the larger ones.

The effect of a secondary transverse load has also been studied, finding that a secondary transverse load increases the critical stress for which the abrupt onset occurs. The failure behavior is also affected by the secondary transverse load, with a totally brittle behavior for a biaxial tensile stress state and a very ductile behavior for tensile-compression stress states. The influence of the secondary transverse loads agrees with others results presented in the literature.

The influence of a second neighbouring fiber has been finally investigated, focusing on the failure pattern. The results showed the ability of the model to predict the coalescence of damage initiated at two different locations, opening perspectives for the study of complex multi-fiber interaction problems involving **shielding** and amplification effects. An additional extension path will recall the enhancement of this modeling framework for dynamic fracture processes, being currently under development.

Acknowledgments

~~The authors acknowledge the funding received from the European Research Council under the European Union's Seventh Framework Programme (FP/2007-2013)/ERC Grant Agreement No. 306622 (ERC Starting Grant "Multi-field and Multi-scale Computational Approach to Design and Durability of Photovoltaic Modules" CA2PVM). IGG and JR acknowledges the support of the projects funded by the Spanish~~

Ministry of Economy and Competitiveness/FEDER (Projects MAT2015-71036-P and MAT2015-71309-P) and the Andalusian Government (Projects of Excellence Nos. TEP-7093 and P12-TEP-1050).

A Numerical implementation of the phase field approach of fracture in the bulk

In the sequel, the main aspects of the numerical implementation of the PF approach of fracture for triggering failure events within the bulk are described within the FEM framework.

The displacements and the phase field variable are interpolated using an isoparametric approach using standard Lagrangian shape functions $N^I(\boldsymbol{\xi})$ defined in the parametric domain $\boldsymbol{\xi} = \{\xi^1, \xi^2\}$ and arranged in the vector \mathbf{N} . Therefore, the interpolation of these fields, their variation and their linearization adopt the following scheme:

$$\mathbf{x} \cong \sum_{I=1}^n N^I \tilde{\mathbf{x}}_I = \mathbf{N}\tilde{\mathbf{x}}; \quad \mathbf{u} \cong \sum_{I=1}^n N^I \mathbf{d}_I = \mathbf{N}\mathbf{d}; \quad \delta \mathbf{u} \cong \sum_{I=1}^n N^I \delta \mathbf{d}_I = \mathbf{N}\delta \mathbf{d}; \quad \Delta \mathbf{u} \cong \sum_{I=1}^n N^I \Delta \mathbf{d}_I = \mathbf{N}\Delta \mathbf{d}, \quad (\text{A.17})$$

$$\vartheta \cong \sum_{I=1}^n N^I \bar{\vartheta}_I = \mathbf{N}\bar{\vartheta}; \quad \delta \vartheta \cong \sum_{I=1}^n N^I \delta \bar{\vartheta}_I = \mathbf{N}\delta \bar{\vartheta}; \quad \Delta \vartheta \cong \sum_{I=1}^n N^I \Delta \bar{\vartheta}_I = \mathbf{N}\Delta \bar{\vartheta}. \quad (\text{A.18})$$

In the Eqs.(A.17)–(A.18), \mathbf{d}_I and $\bar{\vartheta}_I$ are the nodal displacement vector and phase field values, respectively, which are arranged at the element level in the vectors \mathbf{d} and $\bar{\vartheta}$

$$\boldsymbol{\varepsilon} \cong \mathbf{B}_d \mathbf{d}; \quad \delta \boldsymbol{\varepsilon} \cong \mathbf{B}_d \delta \mathbf{d}; \quad \Delta \boldsymbol{\varepsilon} \cong \mathbf{B}_d \Delta \mathbf{d} \quad (\text{A.19})$$

Moreover, the spatial gradient of the phase field variable can be approximated as follows:

$$\nabla_{\mathbf{x}} \vartheta \cong \mathbf{B}_\vartheta \bar{\vartheta}; \quad \nabla_{\mathbf{x}}(\delta \vartheta) \cong \mathbf{B}_\vartheta \delta \bar{\vartheta}; \quad \nabla_{\mathbf{x}}(\Delta \vartheta) \cong \mathbf{B}_\vartheta \Delta \bar{\vartheta}, \quad (\text{A.20})$$

being \mathbf{B}_ϑ a phase field compatibility-like operator.

The discrete form of Eq.(6) at the element level, being denoted by the superscript el , renders

$$\begin{aligned} \delta \tilde{H}_b^{el}(\mathbf{d}, \delta \mathbf{d}, \bar{\vartheta}, \delta \bar{\vartheta}) &= \delta \mathbf{d}^T \left\{ \int_{\mathcal{B}^{el}} \left[\left((1-\vartheta)^2 + \mathcal{K} \right) \mathbf{B}_d^T \boldsymbol{\sigma}_+ + \mathbf{B}_d^T \boldsymbol{\sigma}_- \right] d\Omega - \int_{\partial \mathcal{B}^{el}} \mathbf{N}^T \bar{\mathbf{t}} d\partial\Omega - \int_{\mathcal{B}^{el}} \mathbf{N}^T \mathbf{f}_v d\Omega \right\} \\ &+ \delta \bar{\vartheta}^T \left\{ \int_{\mathcal{B}^{el}} -2(1-\vartheta) \mathbf{N}^T \psi_+^e(\boldsymbol{\varepsilon}) d\Omega + \int_{\mathcal{B}^{el}} \mathcal{G}_{cl}^{bl} \left(\mathbf{B}_\vartheta^T \nabla_{\mathbf{x}} \vartheta + \frac{1}{l^2} \mathbf{N}^T \bar{\vartheta} \right) d\Omega \right\} \\ &= \delta \mathbf{d}^T \mathbf{f}_d^b + \delta \bar{\vartheta}^T \mathbf{f}_\vartheta^b \end{aligned} \quad (\text{A.21})$$

where

$$\mathbf{f}_{d,\text{int}}^b = \int_{\mathcal{B}^{el}} \left[\left((1-\vartheta)^2 + \mathcal{K} \right) \mathbf{B}_d^T \boldsymbol{\sigma}_+ + \mathbf{B}_d^T \boldsymbol{\sigma}_- \right] d\Omega, \quad (\text{A.22})$$

$$\mathbf{f}_{d,\text{ext}}^b = \int_{\partial \mathcal{B}^{el}} \mathbf{N}^T \bar{\mathbf{t}} d\partial\Omega + \int_{\mathcal{B}} \mathbf{N}^T \mathbf{f}_v d\Omega, \quad (\text{A.23})$$

$$\mathbf{f}_\vartheta^b = \int_{\mathcal{B}^{el}} -2(1-\vartheta) \mathbf{N}^T \psi_+^e(\boldsymbol{\varepsilon}) d\Omega + \int_{\mathcal{B}^{el}} \mathcal{G}_{cl}^{bl} \left[\mathbf{B}_\vartheta^T \nabla_{\mathbf{x}} \vartheta + \frac{1}{l^2} \mathbf{N}^T \bar{\vartheta} \right] d\Omega. \quad (\text{A.24})$$

The vectors $\mathbf{f}_{d,\text{int}}^b$ and $\mathbf{f}_{d,\text{ext}}^b$ correspond to the internal and residual vectors associated with the displacement field, whilst \mathbf{f}_ϑ^b stands for the residual vector of the phase field.

The linearization of the previous residual vector yields to the following system (Nguyen, Yvonnet, Zhu, Bornert & Chateau 2016, Nguyen, Yvonnet, Bornert & Chateau 2016, Ambati, Gerasimov & De Lorenzis 2015):

$$\begin{bmatrix} \mathbf{K}_{dd}^b & \mathbf{0} \\ \mathbf{0} & \mathbf{K}_{\vartheta\vartheta}^b \end{bmatrix} \begin{bmatrix} \Delta \mathbf{d} \\ \Delta \vartheta \end{bmatrix} = \begin{bmatrix} \mathbf{f}_{d,\text{ext}}^b \\ \mathbf{0} \end{bmatrix} - \begin{bmatrix} \mathbf{f}_{d,\text{int}}^b \\ \mathbf{f}_\vartheta^b \end{bmatrix}. \quad (\text{A.25})$$

The system given in Eq. (A.25) is solved in Jacobi-type solution scheme in line with (Miehe, Hofacker & Welschinger 2010), though the fully coupled system can be computed via the incorporation of a viscous term in order to guarantee the convexity of the corresponding formulation. The particular form of the tangent matrices \mathbf{K}_{dd}^b , $\mathbf{K}_{d\vartheta}^b$, $\mathbf{K}_{\vartheta d}^b$ y $\mathbf{K}_{\vartheta\vartheta}^b$ are not included in the present manuscript for conciseness reasons.

B Variational formulation and numerical implementation of the interface element compatible with the PF approach of fracture

This Appendix presents the variational formulation regarding the interface contribution to the total functional of the system given in Eq. (10). Complying with a standard Galerkin procedure, the weak form of the interface contribution reads

$$\delta \Pi_{\Gamma_i}(\mathbf{u}, \delta \mathbf{u}, \vartheta, \delta \vartheta) = \int_{\Gamma_i} \left(\frac{\partial \mathcal{G}^i(\mathbf{u}, \vartheta)}{\partial \mathbf{u}} \delta \mathbf{u} + \frac{\partial \mathcal{G}^i(\mathbf{u}, \vartheta)}{\partial \vartheta} \delta \vartheta \right) d\Gamma, \quad (\text{B.26})$$

In Eq.(B.26), $\delta \mathbf{u}$ denotes the admissible kinematic field vector function ($\mathfrak{U}^u = \{\delta \mathbf{u} \mid \mathbf{u} = \bar{\mathbf{u}} \text{ on } \partial \mathcal{B}_u, \mathbf{u} \in \mathcal{H}^1\}$), whereas $\delta \vartheta$ identifies the approximation functions of the phase field variable ($\mathfrak{U}^\vartheta = \{\delta \vartheta \mid \delta \vartheta = 0 \text{ on } \Gamma_b, \vartheta \in \mathcal{H}^0\}$).

The discretization of the previous variational form can be carried out within the context of the FEM through the use of standard isoparametric elements. Without loss of generality, we adopt a first-order interpolation scheme for the kinematic and the phase field variables. Thus,

\mathbf{d} represents the nodal-based displacement field and $\bar{\mathfrak{d}}$ denotes the nodal-based phase field, both vectors being defined at the element level for the corresponding numerical implementation.

Accordingly, the discrete form of Eq.(B.26) at the element level Γ_i^{el} ($\Gamma_i \sim \bigcup \Gamma_i^{el}$) adopts the form:

$$\delta \tilde{\Pi}_{\Gamma_i^{el}}(\mathbf{d}, \delta \mathbf{d}, \bar{\mathfrak{d}}, \delta \bar{\mathfrak{d}}) = \int_{\Gamma_i^{el}} \left(\frac{\partial \mathcal{G}^i(\mathbf{d}, \bar{\mathfrak{d}})}{\partial \mathbf{d}} \delta \mathbf{d} + \frac{\partial \mathcal{G}^i(\mathbf{d}, \bar{\mathfrak{d}})}{\partial \bar{\mathfrak{d}}} \delta \bar{\mathfrak{d}} \right) d\Gamma, \quad (\text{B.27})$$

where $\mathcal{G}^i = \mathcal{G}_I^i + \mathcal{G}_{II}^i$:

The displacement vector between the crack flanks along the interface is characterized by the gap vector, \mathbf{g} . The discrete form of the gap vector for each point of Γ_i^{el} can be computed as the difference between the displacements of opposite points along the interface, which can be obtained from the nodal displacements \mathbf{d} multiplied by the average matrix \mathbf{L} and the interpolation matrix \mathbf{N} :

$$\mathbf{g} = \mathbf{NLd} = \hat{\mathbf{B}}_{\mathbf{d}} \mathbf{d}, \quad (\text{B.28})$$

identifying $\hat{\mathbf{B}}_{\mathbf{d}} = \mathbf{NL}$ the interface compatibility operator.

The constitutive law at the interface requires the consideration of a local setting, which is defined by the normal and tangential unit vectors (Paggi & Wriggers 2012). Correspondingly, the gap vector in the global setting (Eq.(B.28)) is multiplied by rotation matrix \mathbf{R} in order to obtain the gap vector in the local setting \mathbf{g}_{loc} :

$$\mathbf{g}_{\text{loc}} \cong \mathbf{Rg} = \mathbf{R}\hat{\mathbf{B}}_{\mathbf{d}} \mathbf{d}. \quad (\text{B.29})$$

In a similar manner, the discrete average phase field variable \mathfrak{d} at the interface (Γ_i^{el}) can be computed at the element level as follows:

$$\mathfrak{d} \cong \mathbf{N}_\mathfrak{d} \mathbf{M}_\mathfrak{d} \bar{\mathfrak{d}} = \hat{\mathbf{B}}_\mathfrak{d} \bar{\mathfrak{d}}, \quad (\text{B.30})$$

where $\mathbf{M}_\mathfrak{d}$ is a matrix for determining the average value of the phase field variable between the interface flanks, and $\hat{\mathbf{B}}_\mathfrak{d} = \mathbf{N}_\mathfrak{d} \mathbf{M}_\mathfrak{d}$ identifies the compatibility operator for the phase field. The particular form of such matrices are derived in (Reinoso & Paggi 2014, Paggi & Reinoso 2017), being omitted here for the sake of brevity.

Then, the discrete variational form renders

$$\begin{aligned} \delta \tilde{\Pi}_{\Gamma_i^{el}}(\mathbf{d}, \delta \mathbf{d}, \bar{\mathfrak{d}}, \delta \bar{\mathfrak{d}}) &= \delta \mathbf{d}^T \int_{\Gamma_i^{el}} \left(\frac{\partial \mathcal{G}^i(\mathbf{d}, \bar{\mathfrak{d}})}{\partial \mathbf{d}} \right)^T d\Gamma + \delta \bar{\mathfrak{d}}^T \int_{\Gamma_i^{el}} \left(\frac{\partial \mathcal{G}^i(\mathbf{d}, \bar{\mathfrak{d}})}{\partial \bar{\mathfrak{d}}} \right)^T d\Gamma \\ &= \delta \mathbf{d}^T \int_{\Gamma_i^{el}} \hat{\mathbf{B}}_{\mathbf{d}}^T \mathbf{R}^T \left(\frac{\partial \mathcal{G}^i(\mathbf{d}, \bar{\mathfrak{d}})}{\partial \mathbf{g}_{\text{loc}}} \right)^T d\Gamma + \delta \bar{\mathfrak{d}}^T \int_{\Gamma_i^{el}} \hat{\mathbf{B}}_\mathfrak{d}^T \left(\frac{\partial \mathcal{G}^i(\mathbf{d}, \bar{\mathfrak{d}})}{\partial \bar{\mathfrak{d}}} \right)^T d\Gamma \end{aligned} \quad (\text{B.31})$$

leading to the residual vectors

$$\mathbf{f}_{\mathbf{d}}^i = \int_{\Gamma_i^{el}} \hat{\mathbf{B}}_{\mathbf{d}}^T \mathbf{R}^T \left(\frac{\partial \mathcal{G}^i(\mathbf{d}, \bar{\mathfrak{d}})}{\partial \mathbf{g}_{\text{loc}}} \right)^T d\Gamma, \quad (\text{B.32a})$$

$$\mathbf{f}_\mathfrak{d}^i = \int_{\Gamma_i^{el}} \hat{\mathbf{B}}_\mathfrak{d}^T \left(\frac{\partial \mathcal{G}^i(\mathbf{d}, \bar{\mathfrak{d}})}{\partial \bar{\mathfrak{d}}} \right)^T d\Gamma. \quad (\text{B.32b})$$

Finally, the consistent linearization of the previous residual vectors allows the computation of the element tangents of the proposed interface formulation:

$$\mathbf{K}_{\mathbf{d}\mathbf{d}}^i = \frac{\partial \mathbf{f}_{\mathbf{d}}^i}{\partial \mathbf{d}} = \int_{\Gamma_i^{el}} \hat{\mathbf{B}}_{\mathbf{d}}^T \mathbf{R}^T \mathbb{C}_{\mathbf{d}\mathbf{d}}^i \mathbf{R} \hat{\mathbf{B}}_{\mathbf{d}} d\Gamma, \quad (\text{B.33a})$$

$$\mathbf{K}_{\mathbf{d}\mathfrak{d}}^i = \frac{\partial \mathbf{f}_{\mathbf{d}}^i}{\partial \bar{\mathfrak{d}}} = \int_{\Gamma_i^{el}} \hat{\mathbf{B}}_{\mathbf{d}}^T \mathbf{R}^T \mathbb{C}_{\mathbf{d}\mathfrak{d}}^i \hat{\mathbf{B}}_\mathfrak{d} d\Gamma, \quad (\text{B.33b})$$

$$\mathbf{K}_{\mathfrak{d}\mathbf{d}}^i = \frac{\partial \mathbf{f}_\mathfrak{d}^i}{\partial \mathbf{d}} = \int_{\Gamma_i^{el}} \hat{\mathbf{B}}_\mathfrak{d}^T \mathbb{C}_{\mathfrak{d}\mathbf{d}}^i \mathbf{R} \hat{\mathbf{B}}_{\mathbf{d}} d\Gamma, \quad (\text{B.33c})$$

$$\mathbf{K}_{\mathfrak{d}\mathfrak{d}}^i = \frac{\partial \mathbf{f}_\mathfrak{d}^i}{\partial \bar{\mathfrak{d}}} = \int_{\Gamma_i^{el}} \hat{\mathbf{B}}_\mathfrak{d}^T \mathbb{C}_{\mathfrak{d}\mathfrak{d}}^i \hat{\mathbf{B}}_\mathfrak{d} d\Gamma, \quad (\text{B.33d})$$

where the interface operators are given by

$$\mathbb{C}_{\mathbf{d}\mathbf{d}}^i = \begin{bmatrix} \hat{\alpha} k_n & 0 \\ 0 & \hat{\beta} k_t \end{bmatrix}, \quad (\text{B.34a})$$

$$\mathbb{C}_{\mathbf{d}\mathfrak{d}}^i = \begin{bmatrix} g_n k_n & \frac{\partial \hat{\alpha}}{\partial \bar{\mathfrak{d}}} & g_t k_t & \frac{\partial \hat{\beta}}{\partial \bar{\mathfrak{d}}} \end{bmatrix}, \quad (\text{B.34b})$$

$$\mathbb{C}_{\mathfrak{d}\mathbf{d}}^i = \begin{bmatrix} g_n k_n & \frac{\partial \hat{\alpha}}{\partial \bar{\mathfrak{d}}} \\ g_t k_t & \frac{\partial \hat{\beta}}{\partial \bar{\mathfrak{d}}} \end{bmatrix}, \quad (\text{B.34c})$$

$$\mathbb{C}_{\mathfrak{d}\mathfrak{d}}^i = \frac{1}{2} g_n^2 k_n \frac{\partial^2 \hat{\alpha}}{\partial \bar{\mathfrak{d}}^2} + \frac{1}{2} g_t^2 k_t \frac{\partial^2 \hat{\beta}}{\partial \bar{\mathfrak{d}}^2}. \quad (\text{B.34d})$$

In the previous expressions $\hat{\alpha}$ y $\hat{\beta}$ are particularized as follows:

$$\hat{\alpha} = \frac{g_{nc,0}^2}{[(1 - \mathfrak{d})g_{nc,0} + \mathfrak{d}g_{nc,1}]^2}, \quad (\text{B.35a})$$

$$\hat{\beta} = \frac{g_{tc,0}^2}{[(1 - \mathfrak{d})g_{tc,0} + \mathfrak{d}g_{tc,1}]^2}. \quad (\text{B.35b})$$

In line with Eq.(A.25), the final derivation endows a coupled system of equations which is solved in a monolithic manner via a Newton-Raphson scheme.

References

- Ambati, M., Gerasimov, T. & De Lorenzis, L. (2015), ‘Phase-field modeling of ductile fracture’, *Computational Mechanics* **55**(5), 1017–1040.
- Arefi, A. & van der Meer, F. P. (2018), ‘Formulation of a consistent pressure-dependent damage model with fracture energy as input’, *Unpublished manuscript under review, TU Delft, Delft* **201**, 1–26.
- Arteiro, A., Catalanotti, G., Melro, A. R., Linde, P. & Camanho, P. P. (2014), ‘Micro-mechanical analysis of the in situ effect in polymer composite laminates’, *Composite Structures* **116**(1), 827–840.
- Arteiro, A., Catalanotti, G., Melro, A. R., Linde, P. & Camanho, P. P. (2015), ‘Micro-mechanical analysis of the effect of ply thickness on the transverse compressive strength of polymer composites’, *Composites Part A: Applied Science and Manufacturing* **79**, 127–137.
- Bažant, Z. P. (2005), *Scaling of Structural Strength*, Elsevier, Amsterdam.
- Bourdin, B., Francfort, G. A. & Marigo, J.-J. (2000), ‘Numerical experiments in revisited brittle fracture’, *Journal of the Mechanics and Physics of Solids* **48**(4), 797–826.
- Carollo, V., Reinoso, J. & Paggi, M. (2017), ‘A 3d finite strain model for intralayer and interlayer crack simulation coupling the phase field approach and cohesive zone model’, *Composite Structures* **182**, 636 – 651.
- Carollo, V., Reinoso, J. & Paggi, M. (2018), ‘Modeling complex crack paths in ceramic laminates: A novel variational framework combining the phase field method of fracture and the cohesive zone model’, *Journal of the European Ceramic Society* **38**(8), 2994 – 3003. Cermodel 2017: Modelling and Simulation Meet Innovation in Ceramics Technology.
- Comi, C. (1999), ‘Computational modelling of gradient-enhanced damage in quasi-brittle materials’, *Mechanics of Cohesive-frictional Materials* **4**(1), 17–36.
- Comi, C. & Perego, U. (2001), ‘Fracture energy based bi-dissipative damage model for concrete’, *International journal of solids and structures* **38**(36), 6427–6454.
- Correa, E., Mantič, V. & Paris, F. (2008), ‘Numerical characterisation of the fibre-matrix interface crack growth in composites under transverse compression’, *Engineering Fracture Mechanics* **75**(14), 4085–4103.
- Correa, E., Paris, F. & Mantič, V. (2014), ‘Effect of a secondary transverse load on the inter-fibre failure under compression’, *Composites Part B: Engineering* **65**, 57–68.
- Correa, E., Paris, F. & Mantič, V. (2013), ‘Effect of the presence of a secondary transverse load on the inter-fibre failure under tension’, *Engineering Fracture Mechanics* **103**, 174 – 189.
- Danzi, F., Fanteria, D., Panettieri, E. & Palermo, M. (2017), ‘A numerical micro-mechanical study of the influence of fibermatrix interphase failure on carbon/epoxy material properties’, *Composite Structures* **159**, 625–635.
- García, I. G., Mantič, V. & Graciani, E. (2015), ‘Debonding at the fibre-matrix interface under remote transverse tension. One debond or two symmetric debonds?’, *European Journal of Mechanics, A/Solids* **53**, 75–88.
- García, I. G., Paggi, M. & Mantič, V. (2014), ‘Fiber-size effects on the onset of fiber-matrix debonding under transverse tension: A comparison between cohesive zone and finite fracture mechanics models’, *Engineering Fracture Mechanics* **115**, 96–110.
- Griffith, A. A. (1921), ‘The phenomena of rupture and flow in solids’, *Philosophical transaction of the royal society of London. Series A. Containing papers of a Mathematical or physical character* **221**, 163–198.
- Hansen-Drr, A. C., de Borst, R., Hennig, P. & Kstner, M. (2019), ‘Phase-field modelling of interface failure in brittle materials’, *Computer Methods in Applied Mechanics and Engineering* **346**, 25 – 42.
- Herráez, M., Mora, D., Naya, F., Lopes, C. S., González, C. & Llorca, J. (2015), ‘Transverse cracking of cross-ply laminates: A computational micromechanics perspective’, *Composites Science and Technology* **110**, 196–204.
- Legarth, B. N. & Yang, Q. (2016), ‘Micromechanical Analyses of Debonding and Matrix Cracking in Dual-Phase Materials’, *Journal of Applied Mechanics* **83**.
- Linse, T., Hennig, P., Kstner, M. & de Borst, R. (2017), ‘A convergence study of phase-field models for brittle fracture’, *Engineering Fracture Mechanics* **184**, 307 – 318.
- Maimí, P., Camanho, P. P., Mayugo, J. A. & Dávila, C. G. (2007), ‘A continuum damage model for composite laminates: {Part I} - Constitutive model’, *Mechanics of materials* **39**, 897–908.
- Mantič, V. (2009), ‘Interface crack onset at a circular cylindrical inclusion under a remote transverse tension. Application of a coupled stress and energy criterion’, *International Journal of Solids and Structures* **46**(6), 1287–1304.
- Mantič, V. & García, I. G. (2012), ‘Crack onset and growth at the fibre-matrix interface under a remote biaxial transverse load. Application of a coupled stress and energy criterion’, *International Journal of Solids and Structures* **49**(17), 2273–2290.
- Melro, A. R., Camanho, P. P., Andrade Pires, F. M. & Pinho, S. T. (2013), ‘Micromechanical analysis of polymer composites reinforced by unidirectional fibres: Part II-Micromechanical analyses’, *International Journal of Solids and Structures* **50**(11-12), 1906–1915.

- Miehe, C., Hofacker, M. & Welschinger, F. (2010), 'A phase field model for rate-independent crack propagation: Robust algorithmic implementation based on operator splits', *Computer Methods in Applied Mechanics and Engineering* **199**(45), 2765 – 2778.
- Miehe, C., Welschinger, F. & Hofacker, M. (2010), 'Thermodynamically consistent phase-field models of fracture: Variational principles and multi-field fe implementations', *International Journal for Numerical Methods in Engineering* **83**(10), 1273–1311.
- Nguyen, T.-T., Yvonnet, J., Bornert, M. & Chateau, C. (2016), 'Initiation and propagation of complex 3d networks of cracks in heterogeneous quasi-brittle materials: direct comparison between in situ testing-microct experiments and phase field simulations', *Journal of the Mechanics and Physics of Solids* **95**, 320–350.
- Nguyen, T.-T., Yvonnet, J., Zhu, Q.-Z., Bornert, M. & Chateau, C. (2016), 'A phase-field method for computational modeling of interfacial damage interacting with crack propagation in realistic microstructures obtained by microtomography', *Computer Methods in Applied Mechanics and Engineering* **312**, 567–595.
- Ortiz, M. & Pandolfi, A. (1999), 'Finite deformation irreversible cohesive elements for three-dimensional crack-propagation analysis', *International Journal for Numerical Methods in Engineering* **44**, 1267–1282.
- Paggi, M., Corrado, M. & Reinoso, J. (2018), 'Fracture of solar-grade anisotropic polycrystalline silicon: A combined phase fieldcohesive zone model approach', *Computer Methods in Applied Mechanics and Engineering* **330**, 123 – 148.
- Paggi, M. & Reinoso, J. (2017), 'Revisiting the problem of a crack impinging on an interface:a modeling framework for the interaction between the phase field approach for brittle fracture and the interface cohesive zone model', *Computer Methods in Applied Mechanics and Engineering* **321**, 145 – 172.
- Paggi, M. & Wriggers, P. (2012), 'Stiffness and strength of hierarchical polycrystalline materials with imperfect interfaces', *Journal of the Mechanics and Physics of Solids* **60**(4), 557–572.
- Puck, A. & Schürmann, H. (2004), 'Failure analysis of FRP laminates by means of physically based phenomenological models', *Failure Criteria in Fibre-Reinforced-Polymer Composites* **3538**(96), 832–876.
- Quintanas-Corominas, A., Maimí, P., Casoni, E., Turon, A., Mayugo, J. A., Guillaumet, G. & Vázquez, M. (2018), 'A 3D transversally isotropic constitutive model for advanced composites implemented in a high performance computing code', *European Journal of Mechanics, A/Solids* **71**, 278–291.
- Reinoso, J., Arteiro, A., Paggi, M. & Camanho, P. (2017), 'Strength prediction of notched thin ply laminates using finite fracture mechanics and the phase field approach', *Composites Science and Technology* **150**, 205 – 216.
- Reinoso, J., Catalanotti, G., Blázquez, A., Areias, P., Camanho, P. & París, F. (2017), 'A consistent anisotropic damage model for laminated fiber-reinforced composites using the 3d-version of the puck failure criterion', *International Journal of Solids and Structures* **126-127**, 37 – 53.
- Reinoso, J. & Paggi, M. (2014), 'A consistent interface element formulation for geometrical and material nonlinearities', *Computational Mechanics* **54**(6), 1569–1581.
- Reinoso, J., Paggi, M. & Linder, C. (2017), 'Phase field modeling of brittle fracture for enhanced assumed strain shells at large deformations: formulation and finite element implementation', *Computational Mechanics* pp. 1–21.
- Rodríguez, M., Molina-Aldareguía, J. M., González, C. & Llorca, J. (2012), 'A methodology to measure the interface shear strength by means of the fiber push-in test', *Composites Science and Technology* **72**(15), 1924–1932.
- Steinke, C. & Kaliske, M. (2018), 'A phase-field crack model based on directional stress decomposition', *Computational Mechanics* .
- Strobl, M. & Seelig, T. (2015), 'A novel treatment of crack boundary conditions in phase field models of fracture', *PAMM* **15**(1), 155–156.
- Tan, W., Naya, F., Yang, L., Chang, T., Falzon, B. G., Zhan, L., Molina-Aldareguía, J. M., González, C. & Llorca, J. (2018), 'The role of interfacial properties on the intralaminar and interlaminar damage behaviour of unidirectional composite laminates: Experimental characterization and multiscale modelling', *Composites Part B: Engineering* **138**, 206–221.
- Tanné, E., Li, T., Bourdin, B., Marigo, J.-J. & Maurini, C. (2018), 'Crack nucleation in variational phase-field models of brittle fracture', *Journal of the Mechanics and Physics of Solids* **110**, 80 – 99.
- Távora, L., Mantić, V., Graciani, E. & París, F. (2011), 'BEM analysis of crack onset and propagation along fiber-matrix interface under transverse tension using a linear elastic-brittle interface model', *Engineering Analysis with Boundary Elements* **35**(2), 207–222.
- Távora, L., Mantić, V., Graciani, E. & París, F. (2016), 'Modelling interfacial debonds in unidirectional fibre-reinforced composites under biaxial transverse loads', *Composite Structures* **136**, 305 – 312.
- Távora, L., Reinoso, J., Castillo, D. & Mantić, V. (2018), 'Mixed-mode failure of interfaces studied by the 2d linear elastic-brittle interface model: Macro-and micro-mechanical finite-element applications in composites', *The Journal of Adhesion* **94**(8), 627–656.
- Totry, E., Molina-Aldareguía, J. M., González, C. & Llorca, J. (2010), 'Effect of fiber, matrix and interface properties on the in-plane shear deformation of carbon-fiber reinforced composites', *Composites Science and Technology* **70**(6), 970–980.
- Turon, A., Camanho, P., Costa, J. & Renart, J. (2010), 'Accurate simulation of delamination growth under mixed-mode loading using cohesive elements: Definition of interlaminar strengths and elastic stiffness', *Composite Structures* **92**(8), 1857 – 1864.
- Van Der Meer, F. P. (2016), 'Micromechanical validation of a mesomodel for plasticity in composites', *European Journal of Mechanics, A/Solids* **60**, 58–69.
- Verhoosel, C. V. & de Borst, R. (2013), 'A phase-field model for cohesive fracture', *International Journal for Numerical Methods in Engineering* **96**(1), 43–62.
- Xu, X.-P. & Needleman, A. (1994), 'Numerical simulations of fast crack growth in brittle solids', *Journal of the Mechanics and Physics of Solids* **42**(9), 1397–1434.
- Zhuang, L., Pupurs, A., Varna, J., Talreja, R. & Ayadi, Z. (2018), 'Effects of inter-fiber spacing on fiber-matrix debond crack growth in unidirectional composites under transverse loading', *Composites Part A: Applied Science and Manufacturing* **109**, 463–471.
- Zhuang, L., Talreja, R. & Varna, J. (2018), 'Transverse crack formation in unidirectional composites by linking of fibre/matrix debond cracks', *Composites Part A: Applied Science and Manufacturing* **107**, 294–303.